

to appear in ApJ, Vol 527, Dec. 10, 1999

Formation and loss of hierarchical structure in two-dimensional MHD simulations of wave-driven turbulence in interstellar clouds

Bruce G. Elmegreen¹

ABSTRACT

Two dimensional compressible magneto-hydrodynamical (MHD) simulations run for ~ 20 crossing times on a 800×640 grid with two stable thermal states show persistent hierarchical density structures and Kolmogorov turbulent motions in the interaction zone between incoming non-linear Alfvén waves. These structures and motions are similar to what is commonly observed in weakly self-gravitating interstellar clouds, suggesting that these clouds get their fractal structures from non-linear magnetic waves generated in the intercloud medium; no internal source of turbulent energy is necessary. The clumps in the simulated clouds are slightly warmer than the interclump medium as a result of magnetic dissipational and compressive heating when the clumps form. Thus the interclump medium has a lower pressure than the clumps, demonstrating that the clumps owe their existence entirely to transient compressive motions, not pressure confinement by the interclump medium. Clump lifetimes increase with size, and are about one sound crossing time.

Two experiments with this model illustrate a possible trigger for star formation during spontaneous cloud evolution driven by self-gravity and increased self-shielding. A first test is of the hypothesis that a low ionization fraction and enhanced magnetic diffusion lead to the disappearance of clumps smaller than an Alfvén wavelength. Two identical models are run that differ only in the magnetic diffusion rate. The results show a significant decrease in the magnetic wave amplitude as the diffusion rate increases, in agreement with expectations for wave damping, but there is virtually no change in the density structure or amplitude of the density fluctuations as a result of this increased diffusion. This is because all of the density fluctuations are essentially sonic in nature, driven by the noise from Alfvén wave motions outside and at the surface of the cloud. These sonic disturbances travel throughout the cloud parallel to the mean field orientation and are not affected by the local magnetic wave dissipation rate. This result implies that low ionization fractions in molecular clouds do not necessarily lead to increased cloud smoothing.

The second experiment tests the hypothesis that enhanced density alone in a self-gravitating cloud leads to wave self-shielding and loss of incident turbulent energy. Three models with identical conditions except for the presence or lack of an imposed plane-parallel gravitational field confirm that externally generated magnetic waves tend to be excluded from the densest regions of self-gravitating clouds, and as a result these clouds show a significant loss of density substructure. This loss of turbulent energy and density substructure may trigger star formation in the relatively quiescent gas pools that contain a thermal Jeans mass or more. Such a model fits well with the hypothesis that the stellar initial mass function comes from the structure of turbulent hierarchical clouds.

¹IBM Research Division, T.J. Watson Research Center, P.O. Box 218, Yorktown Heights, NY 10598, USA,
bge@watson.ibm.com

Subject Headings: ISM: clouds — ISM: kinematics and dynamics — ISM: structure — MHD — stars: formation — turbulence

1. Introduction

The hierarchical or fractal nature of interstellar clouds has been proposed to result from turbulence because of the expected compression from pervasive supersonic flows, and because of the similarity between cloud structure and the morphology of laboratory turbulence (von Weizsäcker 1951; Sasao 1973; Dickman 1985; Scalo 1985, 1987, 1990; Falgarone 1989; Falgarone & Phillips 1990; Falgarone, Phillips, & Walker 1991; Stutzki, et al. 1991; Mandelbrot 1983; Sreenivasan 1991).

There are several important differences between interstellar and laboratory fluids, however (Scalo 1987; Elmegreen 1993a). The interstellar structure comes from variations in the total gas density, while the laboratory structure is usually in some tracer of fluid motions, such as smoke particles or droplets, with the background density nearly uniform. The interstellar case is also highly magnetic, with the likely inhibition of some torsional motions from magnetic tension. Laboratory turbulence is highly vertical. Thus, the analogy between interstellar and laboratory turbulence is not perfect, even though the resulting structures are somewhat similar.

The purpose of this paper is to demonstrate that interacting non-linear magnetic waves provide a physical mechanism for interstellar turbulence that generates whole clouds and the fractal structures inside of clouds without internal sources or any special (e.g., power-law) initial conditions. Computer simulations in two dimensions show cloud and clump formation at a rapidly cooled, compressed interface between incoming streams of shear Alfvén waves. The resulting structures have power-law characteristics in both space and velocity. Goldreich & Sridhar (1995) also considered turbulence driven by shear Alfvén wave interactions, but treated only the incompressible case. Our results imply that molecular cloud turbulence and clumpy structures do not depend on star formation for their generation. They can arise instead from a variety of energy sources outside the cloud, and get transmitted to the region where the cloud forms along mildly non-linear magnetic waves.

The results also imply that a magnetic field is important for general interstellar turbulence: it distributes the energy from stars and other sources over large regions at supersonic speeds, and it converts this energy via non-linear wave mixing into clouds and clumps spanning a wide range of scales. Intercloud wave damping should not prevent this energy redistribution because the intercloud wave speed is fast and the energy sources are relatively infrequent, making the intercloud wavelength long, perhaps many tens of parsecs. Non-linear damping tends to occur on the scale of a wavelength when the perturbation speed is comparable to the Alfvén speed (Zweibel & Josafatsson 1983; Goldreich & Sridhar 1995). It occurs on longer scales when the perturbation speeds are sub-Alfvénic, as is the case for the models here.

The magnetic field is more important for simulations of interstellar turbulence that use a time-dependent energy equation, as is the case here, than it is for simulations that use a fixed adiabatic index to relate pressure and density. The fixed index has an artificial energy source upon decompression that is not present when the full energy equation is used. As a result, waves and turbulent energy can travel great distances without needing a magnetic field when there is a fixed adiabatic index, but they can hardly disperse at all in the field-free case when the full energy equation is used (Elmegreen 1997b, hereafter Paper I).

In a second part of this paper, we experiment with the hierarchical structures that result from

turbulence to try to understand how diffuse and translucent clouds, which always seem to have tiny clumps down to substellar scales, make the conversion to star-forming clouds that have stellar-mass dense cores. Of course, self-gravity is ultimately important for this conversion, but the presence of sub-stellar clumps in all diffuse clouds implies that as long as turbulence is strong, the stellar-mass clumps that form can always be sheared and sub-divided into even smaller pieces, preventing self-gravity from dominating turbulent pressures on stellar scales (e.g., Padoan 1995). This effect of turbulence is most clearly revealed by the systematic decrease in the ratio of the clump mass to the turbulent Jeans mass on decreasing scales in molecular clouds (Bertoldi & McKee 1992; Falgarone, Puget, & Péault 1992; Vazquez-Semadeni, Ballesteros-Paredes, & Rodriguez 1997). Such a decrease follows directly from the Larson (1981) scaling laws (see Elmegreen 1998). How can stars ever form in a turbulent medium if non-linear motions always break up the structures into smaller, more weakly self-gravitating pieces? The answer must be that star formation begins only after the sub-stellar pieces lose their turbulence and smooth out into larger mass clumps.

One implication of this model is that fragmentation is not the key to star formation: star-forming clouds are already fragmented as a remnant of their pre-star formation turbulence. The *key to star formation is the smoothing of these fragments into stagnant pools larger than a thermal Jeans mass* (Elmegreen 1999). In an extended, well-connected, magnetic medium, turbulent dissipation alone is not enough to initiate this process, because there is a constant flux of turbulent energy into any particular region from waves and motions on larger scales. Only when this external flux stops can the agitated motions begin to decay locally, and only after this decay can the density substructure begin to disappear, allowing stars to form at the thermal Jeans mass and larger.

With this star formation model in mind, we ran several simulations that experiment with possible causes of increased cloud smoothing. One lowers the ionization fraction and thereby decouples the magnetic waves from the gas (Mouschovias 1991; Myers 1998). Another introduces a density gradient from a fixed gravitational potential in order to exclude externally generated waves. The results of these experiments are discussed in Sections 4 and 5. It seems that *the mere condensation of a cloud resulting from bulk self-gravity is enough to initiate star formation in Jeans-mass or larger pieces by excluding external non-linear waves*.

Aside from these applications to star formation, the primary goal of the present work is to demonstrate that interstellar clouds and their hierarchically clumpy substructures can arise as transient objects in the converging parts of supersonic turbulent flows. The general concept that supersonic turbulence can produce density structure has been around for a long time, but specific applications to interstellar clouds were not taken seriously until recently. The early work by Sasao (1973) on this topic was overwhelmed by the more obvious notion that HII regions (Hills 1972; Bania & Lyon 1980), supernovae (Cox & Smith 1974; Salpeter 1976; McKee & Ostriker 1977) and combinations of these pressures (Tenorio-Tagle & Bodenheimer 1988) directly make clouds behind moving shock fronts. Indeed there is a lot of evidence for the bubble structures that are expected from these centralized pressure sources (Brand & Zealey 1975). In addition, thermal instabilities (Field, Goldsmith & Habing 1969) were proposed to make diffuse clouds, while magnetic and gravitational instabilities (Parker 1966; Goldreich & Lynden-Bell 1965) were proposed to make giant clouds, particularly the kpc-size condensations in spiral arms (Elmegreen 1979). Everything in between was supposed to be made by the build-up and dispersal cycle of collisional agglomeration (e.g., Field & Saslaw 1965; Kwan 1979).

The importance of turbulence as a structuring agent has now reemerged in the astronomical literature. This change slowly followed several key observations, including the recognition of correlated motions in molecular clouds (Larson 1981) and of pervasive small scale structure in diffuse (Low et al. 1984; Scalo

1990), ionized (Spangler 1998), and molecular clouds (e.g., Falgarone, Phillips, & Walker 1991; Stutzki et al. 1998; Falgarone et al. 1998). Correlated motions and power-law structures also appear in HI surveys (Green 1993; Lazarian 1995; Stanimirovic et al. 1999; Lazarian & Pogosyan 1999). LaRosa, Shore & Magnani (1999) found correlated motions in a translucent cloud and suggested the driving source was outside, as in the present model.

Astrophysical models of cloud formation also reflected this change by including turbulence compression as one of several mechanisms (see reviews in Elmegreen 1993a, 1996). Star formation theory changed as well, e.g., by considering not only the influence of converging turbulent flows on the gravitational stability of clumps (Hunter & Fleck 1982), but also the stability of clumps that specifically formed by this compression and whose lifetimes were consequently very short (Elmegreen 1993b). Recent emphasis on cloud formation in turbulence-induced flows is in Ballesteros-Paredes, Vazquez-Semadeni & Scalo (1999), with an application to the Taurus clouds by Hartmann, Ballesteros-Paredes, & Vazquez-Semadeni, et al. (1999). The high latitude clouds (Magnani, Blitz, & Mundy 1995) may be examples as well, because of their short lives. A generalization of turbulence structures to include both cloud and intercloud media is in Elmegreen (1997a).

Other astrophysical turbulence simulations have addressed different problems. In a series of papers, Vazquez-Semadeni, Passot & Pouquet (1995, 1996), Passot, Vazquez-Semadeni, & Pouquet (1995), and Vazquez-Semadeni, Ballesteros-Paredes, & Rodriguez (1997) studied the properties of clouds and star formation in a turbulence model with star formation heating, gaseous gravity, rotation, magnetism, and other effects, to simulate a galactic-scale piece of the interstellar medium.

Gammie, & Ostriker (1996) used a 1D simulation to show that forces parallel to the mean field can support a cloud against self-gravity. Stone, Ostriker, & Gammie (1998) and MacLow, et al. (1998) found the rate of energy dissipation in 3D supersonic MHD turbulence to be about the same as in turbulence without magnetic fields, and suggested that energy input from embedded stars or other sources was necessary to maintain cloud structure for more than a crossing time. Vazquez-Semadeni (1994), Nordlund, & Padoan (1998), and Scalo et al. (1998) found a log-normal probability density distribution generated by compressible turbulence. Hierarchical turbulent structures like those produced here have also been generated in the wakes behind shocked clouds (Klein, McKee & Colella 1994; Mac Low et al. 1994; Xu & Stone 1995).

Padoan (1998) proposed that interstellar turbulence is super-Alfvénic in order to get significant compression. This is different from the cases considered here, where all the cloud motions are sub-Alfvénic. We believe his application of MHD results to interstellar turbulence is inappropriate because the interstellar structure is hierarchically clumped, and super-Alfvénic turbulence can only be super-Alfvénic for one level in a hierarchy of structures. Once a region is compressed, it becomes sub-Alfvénic because the magnetic pressure increases much more than the thermal. Thus the process of turbulence compression would stop after only one level in his model and could never get the observed hierarchical structures. In the MHD simulations discussed here, the hierarchical structure comes from sonic and slightly supersonic motions along the field, driven by transverse magnetic waves. Such sonic disturbances can divide the gas into very small pieces regardless of the local field strength.

The present work in two-dimensions is an extension of the same cloud formation problem considered in one-dimension earlier, first with the simple demonstration that non-linear transverse Alfvén waves push the gas along and make high density structures when they interact (Elmegreen 1990), and then with randomly driven transverse waves at the ends of a 1D grid making hierarchical density structures in the remote regions between (Elmegreen 1991, and Paper I). The first 2D simulations of clumpy structure from

interacting magnetic waves were in Yue et al. (1993).

This 1D compression between wave sources is analogous to the “turbulent cooling flow” discussed by Myers & Lazarian (1998), but it is not exactly the same. Here a dense region forms because of a convergence and high pressure from external magnetic waves and the thermal cooling that follows at the compressed interface. Turbulent dissipation at the interface is not as important as thermal cooling for this density enhancement. The turbulent cooling envisioned by Myers & Lazarian leads to a macroscopic thermal instability (Struck-Marcell & Scalo 1984; Tomisaka 1987; Elmegreen 1989). If this were to operate in addition to the thermal variations modeled here, then the density enhancement in the converging region would be even larger than what thermal effects alone give. However, the turbulent energy in the cloud is continuously resupplied from outside, and it gets in easily until the cloud density contrast becomes large (Sect. 5). As a result, the internal turbulent energy does not decrease much for small perturbations in the density, and there is no runaway turbulent cooling in our models.

In what follows, we discuss the MHD algorithm and tests of the numerical code in Section 2.1. This method of solving fluid equations is new to the astronomy community, so we summarize the essential points in some detail (it was used also in Paper I for 1D turbulence, but the equations were not given there). In section 3, the basic MHD simulation that generates hierarchical and scale-free structure from turbulence is discussed. Models with enhanced magnetic diffusion are in section 4 and models with imposed, plane-parallel gravity are in section 5.

2. The relaxation algorithm of Jin & Xin

2.1. Introduction

The relaxation algorithm developed by Jin & Xin (1995) has been adapted here to include magnetic fields. We also added heating and cooling rates to the energy equation to give two stable thermal states. This is analogous to what we did for the one dimensional problem (Paper I).

The Jin & Xin method is a way to solve systems of conservation equations with no need for artificial viscosity in the equation of motion. It does this by dividing the primary equations of motion and continuity into three equations,

$$\frac{\partial \mathbf{S}}{\partial t} + \frac{\partial \mathbf{v}}{\partial x} + \frac{\partial \mathbf{w}}{\partial y} = 0, \quad (1)$$

$$\frac{\partial \mathbf{v}}{\partial t} + A \frac{\partial \mathbf{S}}{\partial x} = -\frac{1}{\epsilon} (\mathbf{v} - \mathbf{F}_x [\mathbf{S}]) \quad (2)$$

$$\frac{\partial \mathbf{w}}{\partial t} + B \frac{\partial \mathbf{S}}{\partial y} = -\frac{1}{\epsilon} (\mathbf{w} - \mathbf{F}_y [\mathbf{S}]). \quad (3)$$

The vector \mathbf{S} is a vector of physical variables consisting of density, momentum density, magnetic field strength, and energy density, as written below. The vectors \mathbf{F}_x and \mathbf{F}_y are the two spatial components of the total forces on each physical variable, which are, in general, functions of the physical variables. The scalar ϵ is a relaxation rate, taken to be a small positive parameter with the dimensions of time, and A and B are diagonal matrices with the dimensions of velocity squared. Vectors \mathbf{v} and \mathbf{w} are intermediate variables that “relax” to the force vectors, \mathbf{F}_x and \mathbf{F}_y , respectively, on the time scale ϵ .

To ensure stability, $A > (\partial \mathbf{F}_x [\mathbf{S}] / \partial \mathbf{S})^2$ and $B > (\partial \mathbf{F}_y [\mathbf{S}] / \partial \mathbf{S})^2$ for all \mathbf{S} , which means that each element of A and B has to equal or exceed the square of the maximum velocity that occurs in the

simulation. For our calculations, we take a constant $a \equiv A^{1/2} = B^{1/2} =$ several times the Alfvén speed in the unperturbed gas.

The Jin & Zin method requires that the physical equations for the problem be written in conservative form (see also Dai & Woodward 1998). It also prescribes how to discretize the spatial and time steps in an efficient and stable way.

2.2. Spatial Discretization

The spatial discretization is done in the manner suggested by Jin & Xin (1995). This is second-order accurate, and follows from van Leer (1979), using a piecewise linear interpolation. The resulting discrete forms of equations 1–3 are, for each component of the vectors \mathbf{S} , \mathbf{v} , \mathbf{F}_x , and \mathbf{F}_y :

$$\frac{\partial}{\partial t} S + D_x(v, S) + D_y(w, S) = 0 \quad (4)$$

$$\frac{\partial}{\partial t} v + a^2 D_x(v, S) = -\frac{1}{\epsilon} (v - F_x[S]), \quad (5)$$

$$\frac{\partial}{\partial t} w + a^2 D_y(w, S) = -\frac{1}{\epsilon} (w - F_y[S]), \quad (6)$$

where the derivatives for v and w are

$$D_x(v_{i,j}, S_{i,j}) = \frac{1}{2\Delta} (v_{i+1,j} - v_{i-1,j}) - \frac{a}{2\Delta} (S_{i+1,j} - 2S_{i,j} + S_{i-1,j}) - \frac{1}{4} (\sigma_{x;i+1,j}^- - \sigma_{x;i,j}^- - \sigma_{x;i,j}^+ + \sigma_{x;i-1,j}^+), \quad (7)$$

$$D_y(w_{i,j}, S_{i,j}) = \frac{1}{2\Delta} (w_{i,j+1} - w_{i,j-1}) - \frac{a}{2\Delta} (S_{i,j+1} - 2S_{i,j} + S_{i,j-1}) - \frac{1}{4} (\sigma_{y;i,j+1}^- - \sigma_{y;i,j}^- - \sigma_{y;i,j}^+ + \sigma_{y;i,j-1}^+). \quad (8)$$

The indices (i, j) represent the (x, y) positions in the computational grid, Δ is a constant spatial step size, a is the maximum velocity for the problem, and σ is a derivative correction, given by

$$\sigma_{x;i,j}^\pm = \frac{1}{\Delta} (v_{i+1,j} \pm aS_{i+1,j} - [v_{i,j} \pm aS_{i,j}]) \phi(\theta_{x;i,j}^\pm) \quad (9)$$

$$\sigma_{y;i,j}^\pm = \frac{1}{\Delta} (w_{i,j+1} \pm aS_{i,j+1} - [w_{i,j} \pm aS_{i,j}]) \phi(\theta_{y;i,j}^\pm) \quad (10)$$

where

$$\theta_{x;i,j}^\pm = \frac{v_{i,j} \pm aS_{i,j} - [v_{i-1,j} \pm aS_{i-1,j}]}{v_{i+1,j} \pm aS_{i+1,j} - [v_{i,j} \pm aS_{i,j}]}, \quad (11)$$

$$\theta_{y;i,j}^\pm = \frac{w_{i,j} \pm aS_{i,j} - [w_{i,j-1} \pm aS_{i,j-1}]}{w_{i,j+1} \pm aS_{i,j+1} - [w_{i,j} \pm aS_{i,j}]}, \quad (12)$$

and

$$\phi(\theta) = \max(0, \min[1, \theta]) \quad (13)$$

is a relatively smooth, slope-limiting function.

2.3. Time Discretization

The time stepping is done with a second-order, total variation diminishing (TVD), Runge-Kutta splitting time discretization that keeps the convection terms explicit and the lower order terms implicit (Jin 1995). We write this discretization method in terms of the current time step, with superscript n , the next time step, with index $n + 1$, and intermediate values with superscripts $*$, $**$, (1) , and (2) (see also Jin & Xin 1995):

$$\mathbf{S}^* = \mathbf{S}^n \quad (14)$$

$$\mathbf{v}^* = \frac{\mathbf{v}^n - \mathbf{F}_x(\mathbf{S}^*) dt/\epsilon}{1 - dt/\epsilon} \quad (15)$$

$$\mathbf{w}^* = \frac{\mathbf{w}^n - \mathbf{F}_y(\mathbf{S}^*) dt/\epsilon}{1 - dt/\epsilon} \quad (16)$$

$$\mathbf{S}^{(1)} = \mathbf{S}^* - D_x(\mathbf{v}^*, \mathbf{S}^*) dt - D_y(\mathbf{w}^*, \mathbf{S}^*) dt \quad (17)$$

$$\mathbf{v}^{(1)} = \mathbf{v}^* - a^2 D_x(\mathbf{v}^*, \mathbf{S}^*) dt \quad (18)$$

$$\mathbf{w}^{(1)} = \mathbf{w}^* - a^2 D_y(\mathbf{w}^*, \mathbf{S}^*) dt \quad (19)$$

$$\mathbf{S}^{**} = \mathbf{S}^{(1)} \quad (20)$$

$$\mathbf{v}^{**} = \frac{\mathbf{v}^{(1)} + \mathbf{F}_x(\mathbf{S}^{**}) dt/\epsilon - 2[\mathbf{v}^* - \mathbf{F}_x(\mathbf{S}^*)] dt/\epsilon}{1 + dt/\epsilon} \quad (21)$$

$$\mathbf{w}^{**} = \frac{\mathbf{w}^{(1)} + \mathbf{F}_y(\mathbf{S}^{**}) dt/\epsilon - 2[\mathbf{w}^* - \mathbf{F}_y(\mathbf{S}^*)] dt/\epsilon}{1 + dt/\epsilon} \quad (22)$$

$$\mathbf{S}^{(2)} = \mathbf{S}^{**} - D_x(\mathbf{v}^{**}, \mathbf{S}^{**}) dt - D_y(\mathbf{w}^{**}, \mathbf{S}^{**}) dt \quad (23)$$

$$\mathbf{v}^{(2)} = \mathbf{v}^{**} - a^2 D_x(\mathbf{v}^{**}, \mathbf{S}^{**}) dt \quad (24)$$

$$\mathbf{w}^{(2)} = \mathbf{w}^{**} - a^2 D_y(\mathbf{w}^{**}, \mathbf{S}^{**}) dt \quad (25)$$

$$\mathbf{S}^{n+1} = \left(\mathbf{S}^n + \mathbf{S}^{(2)} \right) / 2 \quad (26)$$

$$\mathbf{v}^{n+1} = \left(\mathbf{v}^n + \mathbf{v}^{(2)} \right) / 2 \quad (27)$$

$$\mathbf{w}^{n+1} = \left(\mathbf{w}^n + \mathbf{w}^{(2)} \right) / 2. \quad (28)$$

The time step has to satisfy $dt \gg \epsilon$ to make the \mathbf{v}^* and \mathbf{w}^* equations stable; we use $dt = 10^{-2}$ and $\epsilon = 10^{-6}$ for the standard and gravitating slab cases, and $dt = 10^{-3}$ and $\epsilon = 10^{-9}$ for the experiment with low magnetic diffusion. (Reasons for these timesteps are given in sections 2.4.5 and 4.)

2.4. Physical Equations in Conservative Form

2.4.1. Mass Conservation

The variables \mathbf{S} , and the force vectors \mathbf{F}_x and \mathbf{F}_y , come from the physical equations written in conservative form, which is $\partial\mathbf{S}/\partial t + \nabla \cdot \mathbf{F} = 0$. The mass conservation equation,

$$\frac{\partial \rho}{\partial t} + \nabla \cdot \rho \mathbf{v} = 0 \quad (29)$$

is already in this form for mass density ρ and velocity vector \mathbf{v} . We rewrite this and other equations in terms of indices j to designate the spatial vector components x and y ,

$$\frac{\partial \rho}{\partial t} + \frac{\partial \rho v_j}{\partial x_j}. \quad (30)$$

Then the first terms in the \mathbf{S} , \mathbf{F}_x and \mathbf{F}_y vectors are

$$S_1 = \rho ; \quad F_1^j = \rho v_j \quad (31)$$

where $j = 1$ for the x component and $j = 2$ for the y component.

2.4.2. Equation of Motion

The equation of motion can be written in the same way, but gravity, viscosity, and perhaps other forces add additional terms to the right hand side:

$$\frac{\partial \mathbf{S}}{\partial t} + \nabla \cdot \mathbf{F} = \mathbf{D}. \quad (32)$$

The viscous terms and gravity are inside \mathbf{D} . We do not include any viscosity in the equations because molecular viscosity is negligible in interstellar clouds; all of the energy dissipation occurs in the cooling term, Λ , which appears in the energy equation. We also ignore self-gravity for simplicity, but some runs have fixed gravity to investigate clumpy structure in regions with smooth density gradients.

To include magnetic diffusion, we write separate equations of motion for the neutrals and ions. For the ions (distinguished by the symbol "+"), the equation of motion is

$$\rho_+ \left(\frac{\partial \mathbf{v}_+}{\partial t} + \mathbf{v}_+ \cdot \nabla \mathbf{v}_+ \right) = -\nabla P_+ + \rho_+ \mathbf{g} + \frac{1}{4\pi} \mathbf{B} \cdot \nabla \mathbf{B} - \frac{1}{8\pi} \nabla \mathbf{B} \cdot \mathbf{B} - n_+ < \sigma a_t > \mu (\mathbf{v}_+ - \mathbf{v}) n \quad (33)$$

where $< \sigma a_t >$ is the ion-neutral thermal collision rate for thermal speed a_t , μ is the reduced ion-neutral mass, n_+ is the charged particle density, n is the total particle density, \mathbf{B} is the magnetic field strength, and \mathbf{g} is the gravitational acceleration. The total mass density of the ions is negligible in interstellar clouds, so the inertial terms can be dropped. Then we get

$$\frac{1}{4\pi} \mathbf{B} \cdot \nabla \mathbf{B} - \frac{1}{8\pi} \nabla \mathbf{B} \cdot \mathbf{B} = n_+ < \sigma a_t > \mu n (\mathbf{v}_+ - \mathbf{v}) \equiv \omega_+ \rho (\mathbf{v}_+ - \mathbf{v}), \quad (34)$$

where ω_+ is defined as a collision rate per unit volume, corrected for reduced mass.

For the neutral particles, the equation of motion is

$$\rho \left(\frac{\partial \mathbf{v}}{\partial t} + \mathbf{v} \cdot \nabla \mathbf{v} \right) = -\nabla P + \rho \mathbf{g} - \omega_+ \rho (\mathbf{v} - \mathbf{v}_+). \quad (35)$$

For this equation, $-\omega_+ \rho (\mathbf{v} - \mathbf{v}_+)$ may be substituted from above to give

$$\rho \left(\frac{\partial \mathbf{v}}{\partial t} + \mathbf{v} \cdot \nabla \mathbf{v} \right) = -\nabla P + \rho \mathbf{g} + \frac{1}{4\pi} \mathbf{B} \cdot \nabla \mathbf{B} - \frac{1}{8\pi} \nabla \mathbf{B} \cdot \mathbf{B}. \quad (36)$$

The ion equation will be used again to write the time evolution of the magnetic field in terms of convective and diffusion terms.

This neutral equation of motion can be converted to the conservative form:

$$\frac{\partial \rho v_i}{\partial t} + \frac{\partial \rho v_i v_j}{\partial x_j} + \frac{\partial}{\partial x_j} \left[\left(p + \frac{B^2}{8\pi} \right) \delta_{ij} - \frac{B_i B_j}{4\pi} \right] = \rho g_i \quad (37)$$

where $\delta_{ij} = 1$ for $i = j$. As a result, the second and third components of S , F , and D , designated by subscripts $i+1 = 2, 3$, are, for spatial coordinate indices $i = 1, 2$ and $j = 1, 2$:

$$S_{i+1} = \rho v_i \quad (38)$$

$$F_{i+1}^j = \rho v_i v_j + \left(p + \frac{B^2}{8\pi} \right) \delta_{ij} - \frac{B_i B_j}{4\pi} \quad (39)$$

$$D_{i+1} = \rho g_i. \quad (40)$$

With this notation, the equation of motion is

$$\frac{\partial S_{i+1}}{\partial t} + \frac{\partial F_{i+1}^j}{\partial x_j} = D_{i+1}, \quad (41)$$

where $j = 1$ and 2 for the x and y components of the force matrix, and $i = 1$ and 2 for the x and y components of the momentum density.

2.4.3. Equation of Magnetic Field Evolution

Magnetic field evolution is given by the convection of ions in the usual way:

$$\frac{\partial \mathbf{B}}{\partial t} = \nabla \times (\mathbf{v}_+ \times \mathbf{B}). \quad (42)$$

This may be written in terms of the neutral velocity \mathbf{v} :

$$\frac{\partial \mathbf{B}}{\partial t} = \nabla \times (\mathbf{v} \times \mathbf{B}) - \nabla \times ([\mathbf{v} - \mathbf{v}_+] \times \mathbf{B}) \quad (43)$$

where $\mathbf{v} - \mathbf{v}_+$ comes from equation (34).

To write this equation in conservative form, we have to expand $\nabla \times (\mathbf{v} \times \mathbf{B})$ and rearrange terms. The result is

$$\frac{\partial B_i}{\partial t} + \frac{\partial}{\partial x_j} [v_j B_i - v_i B_j] + \frac{\partial}{\partial x_j} [(v_{j+} - v_j) B_i - (v_{i+} - v_i) B_j] = 0. \quad (44)$$

The last two terms come from equation (34), which may be re-written as

$$v_{i+} - v_i = \frac{1}{\omega_+ \rho} \left[\frac{1}{4\pi} \frac{\partial (B_k B_i - 0.5 \delta_{ik} B^2)}{\partial x_k} \right]. \quad (45)$$

This form of the magnetic field evolution equation indicates that the computational variables are, for $i = 1, 2$,

$$S_{i+4} = B_i, \quad (46)$$

$$F_{i+4}^j = v_j B_i - v_i B_j \quad (47)$$

and

$$D_{i+4} = -\frac{\partial}{\partial x_j} [(v_{j+} - v_j)B_i - (v_{i+} - v_i)B_j] \quad (48)$$

where equation (45) has to be used as well. Thus the equation of magnetic field evolution becomes similar to equation (41) for $i = 1, 2$,

$$\frac{\partial S_{i+4}}{\partial t} + \frac{\partial F_{i+4}^j}{\partial x_j} = D_{i+4}. \quad (49)$$

2.4.4. Energy Equation

The energy equation in conventional form is

$$\frac{\partial U}{\partial t} + \mathbf{v} \cdot \nabla U + (U + p)\nabla \cdot \mathbf{v} = \Gamma - \Lambda, \quad (50)$$

where

$$U = \frac{p}{\gamma - 1} \quad (51)$$

is the energy density, p is the thermal pressure, Γ and Λ are the thermal heating and cooling rates, and $\gamma = 5/3$ is the ratio of specific heats for a monatomic or cold molecular gas. Note that these are the fundamental physical variables, and not effective variables, such as turbulent pressure or effective γ , which is sometimes used for shock fronts to automatically include heating and cooling behind the shock. Here the computer code generates by itself what we have come to think of as “turbulent pressure,” and the heating and cooling terms determine the relation between temperature and pressure in a self-consistent way.

The energy equation is converted into conservative form by adding it to the dot product of the velocity with the equation of motion, and then substituting from other equations. The result has the same general form as before, now written with subscript 6 because for a two dimensional problem, the energy equation is the 6th component of the general vector equation:

$$\frac{\partial S_6}{\partial t} + \frac{\partial F_6^j}{\partial x_j} = D_6. \quad (52)$$

where

$$S_6 = U + 0.5\rho v^2 + B^2/(8\pi) \quad (53)$$

is the total energy,

$$F_6^j = v_j [U + p + 0.5\rho v^2 + B^2/(4\pi)] - B_j B_i v_i/(4\pi) \quad (54)$$

is the energy flux, and

$$D_8 = -\frac{B_i}{4\pi} \frac{\partial}{\partial x_j} [X_j B_i - X_i B_j] + \Gamma - \Lambda + \rho v_i g_i, \quad (55)$$

where

$$X_j = \frac{1}{\omega_+ \rho} \left[\frac{1}{4\pi} \frac{\partial (B_k B_j - 0.5\delta_{jk} B^2)}{\partial x_k} \right]. \quad (56)$$

Throughout these derivations, we have used the convention that repeated indices are summed.

The heating and cooling terms are designed to give two stable temperature states and an unstable state between them. This is done by taking

$$\Gamma - \Lambda = -\Gamma_0 \rho p C (C - 0.5) (C - 1) / 0.04811 \quad (57)$$

where $C = \log(p/\rho)$. For large temperatures, $C \sim 1$, the quantity $\Gamma - \Lambda$ is zero and decreasing with increasing C , so the region cools if $C > 1$ and heats up if $C < 1$; this is stable behavior with equilibrium at $C = 1$. For low temperature, $C \sim 0$, $\Gamma - \Lambda \sim 0$ and decreasing again, so the region is stable there too. At intermediate temperatures, where $C \sim 0.5$, $\Gamma - \Lambda$ increases with C , so $C > 0.5$ leads to more heating and a further increase in C , while $C < 0.5$ leads to more cooling and a further decrease in C ; this is unstable behavior. The equilibrium temperatures correspond to $p/\rho = 1$ and 10. For comparison, the initial temperature in all of our simulations corresponds to the stable solution, $p/\rho = 1$, and the initial Alfvén speed, $B/(4\pi\rho)^{1/2}$, is 10. The coefficient 0.04811 in $\Gamma - \Lambda$ makes the peak values of the cubic part, $-C(C - 0.5)(C - 1)$, equal to -1 at $\log p/\rho = 0.211$ and $+1$ at $\log p/\rho = 0.789$.

The constant $\Gamma_0 = 10^{-3}$ determines the cooling time. If we write the magnetic field-free equation of energy as $Dp/Dt = (\gamma p/\rho) D\rho/Dt + (\gamma - 1)(\Gamma - \Lambda)$, then the cooling time is $t_{cool} = ([\gamma - 1]\Gamma_0\rho)^{-1}$. Initially, this is $3/(2\Gamma_0)$ for $\gamma = 5/3$ and $\rho = 1$, and this is 1500 for $\Gamma_0 = 10^{-3}$. This is about the duration of the simulations, so the local cooling time is approximately the simulation run time divided by the density.

2.4.5. Discussion

This completes the derivation of the physical equations in conservative form. The variables actually used by the computer are the S variables, so all these equations for F and D have to be written in terms of these S variables. This means, for example, that v_1 in an equation has to be written as S_2/S_1 , and so on. The S variables are initialized after consideration of the physical problem, \mathbf{v} is initialized to \mathbf{F}_x , and \mathbf{w} is initialized to \mathbf{F}_y . Then the S variables are incremented in time, as discussed in Section 2.3.

The unit of time in the simulation is equal to the crossing time of a coordinate cell ($dx = dy = 1$) at a velocity given by the initial ratio of $P/\rho = 1$. The time step size in the simulation is much smaller than this time unit, because many types of motions are faster than 1 velocity unit. Initial Alfvén waves move at a speed of 10 velocity units, sound waves in the warm phase move at a speed of $10^{1/2}\gamma = 5.3$, and Alfvén waves in the warm phase, where the density is low ($\rho \sim 0.1$) move at $10/(\rho)^{1/2} \sim 30$. Thus we use a time step of 0.01, which is short enough to follow all of these motions.

The equations were solved on an IBM SP parallel computer, with computational space divided up between processors, and communication between processors done with message passing (MPI). A typical run of 1536 time units, which is 153600 time steps, on a grid of 800×640 , with magnetic diffusion, heating and cooling, took about 150 node-days on an IBM SP with the Power2sc processor. We report three of these runs here, one without gravity and two with a fixed gravitational potential, plus two other runs on a 400×320 grid to test the importance of magnetic diffusion.

2.5. Tests

2.5.1. Linear Waves

Several tests were run to check the accuracy of the MHD solutions. In all tests, magnetic diffusion was turned off and $\Gamma - \Lambda$ was set equal to zero. All simulations used 64-bit floating point accuracy.

In a simulation with 800 cells and a constant value of the magnetic field strength and density, a perturbation was given to the velocity in a direction perpendicular to the field at a grid position halfway

between the two boundaries. The perturbation was very low in amplitude (10^{-2} times the sound speed), and it had a sinusoidal time dependence to generate a smooth Alfvén wave. The average wavelength of the wave was measured to be within the factor 9.6×10^{-5} of the theoretical prediction (200 cells), indicating that the linearized Alfvén speed has this accuracy.

2.5.2. Shock jump conditions

In another simulation with the same initial conditions, a larger perpendicular velocity was applied to the same centralized grid point for one sinusoidal cycle, and the resulting two diverging waves quickly steepened into shock fronts as they moved away from this point (cf. Fig. 1). The shocks continued along the field lines gathering mass and decreasing in amplitude. The accuracy of the jump conditions was determined from the rms dispersion of the various measures of the shock speed:

$$\xi_1 = [m_y]/[\rho], \quad (58)$$

$$\xi_2 = \frac{[m_y^2/\rho] + [p] + [B_x^2]/8\pi}{[m_y]}, \quad (59)$$

$$\xi_3 = \frac{[m_x m_y/\rho] - B_x [B_y]/4\pi}{[m_x]}, \quad (60)$$

and

$$\xi_4 = \frac{[B_x m_y/\rho] - B_y [m_x/\rho]}{[B_x]}, \quad (61)$$

where $m_y = \rho v_y$ and $m_x = \rho v_x$ are the momentum densities parallel and perpendicular to the initial field (equal to S_3 and S_2 in the notation of Eq. 38). The time evolution of the perpendicular momentum, m_x , is in figure 1.

The amplitude of the perturbation was such that the velocity of the resulting motion was intermediate between the sound speed and the Alfvén speed (1 and 10 in these units, respectively). This is the regime of the cloud simulations discussed in the rest of this paper, based on observations of velocities and Alfvén speeds in the interstellar medium.

The jump condition expressions given above are the shock speeds from the mass flux parallel to the field and to the direction of propagation of the wave, the parallel momentum flux, perpendicular momentum flux, and perpendicular magnetic field flux, respectively. These quantities are evaluated at the grid point with the maximum density behind the shock. The shock jump differences denoted by square brackets [...] are determined from the differences between the values of various quantities at the density peak and values at points ahead of the shocks by 20 grid spaces (this number 20 does not matter, as long as it places the preshock condition in the unperturbed area). The relative rms deviation between all four determinations of the shock velocity is a measure of the accuracy of the jump conditions. This relative rms value is shown in Figure 1 as a plus symbol, using the right hand axis. It is typically 1% or less, indicating that the shock jump conditions are satisfied to within this accuracy. Note that the shock fronts are not sharp at late times in this test because the velocity is less than the Alfvén speed (compare to Fig. 4 below).

Analogous simulations with perturbations perpendicular to the initial uniform field gave the same order of magnitude for the accuracy of the jump conditions.

2.5.3. Measurement of the $\nabla \cdot \mathbf{B} = 0$ error

Another important test is for the error in $\nabla \cdot \mathbf{B} = 0$ to be small. Evans & Hawley (1988), Stone & Norman (1992), and Dai & Woodward (1998) developed codes that explicitly force $\nabla \cdot \mathbf{B} = 0$, but our code only gives $\nabla \cdot \mathbf{B} = 0$ to within the numerical accuracy determined by the grid and time stepping. Figure 2 shows the average and rms values of $\nabla \cdot \mathbf{B}/(\mathbf{B} \cdot \mathbf{B})^{1/2}$ inside the computational grid of the 2D-MHD simulation discussed in section 3. For this evaluation, we considered both the total grid, measuring 800×640 with the 800 cell direction parallel to the initial field, and the central portion of this grid, from positions 120 to 680 parallel to the field (outside the sources of excitation for the waves) and 0 to 640 perpendicular to \mathbf{B} . The values of $\nabla \cdot \mathbf{B}/(\mathbf{B} \cdot \mathbf{B})^{1/2}$ are for the latter, shown at intervals of one time unit, which is 100 time steps, for 1536 time units overall.

Both the average and the rms values of $\nabla \cdot \mathbf{B}/(\mathbf{B} \cdot \mathbf{B})^{1/2}$ are steady throughout the calculation. The average value is $\pm 5 \times 10^{-8}$ and the rms is $\sim 7 \times 10^{-5}$. The average is smaller than the rms because this quantity fluctuates over positive and negative values. There is no systematic drift for either the average or the rms.

The lack of any systematic drift in $\nabla \cdot \mathbf{B}/(\mathbf{B} \cdot \mathbf{B})^{1/2}$ over time, and the smallness of its value, imply that stochastic monopoles, which are most likely the result of round-off errors in calculating \mathbf{B} and other variables, are transient and so few in number that they do not affect the code. Considering that the 560×640 grid in which $\nabla \cdot \mathbf{B}/(\mathbf{B} \cdot \mathbf{B})^{1/2}$ was measured has 3.6×10^5 cells, there are on average $(7 \times 10^{-5}) \times (3.6 \times 10^5) \sim 25$ monopoles at any one time, with positive and negative signs canceling each other to give a net monopole number of less than $(5 \times 10^{-8}) \times (3.6 \times 10^5) \sim 0.02$. Even though the code is not designed to force the monopole number to be zero at all times, this number is still so small that any effects from non-zero $\nabla \cdot \mathbf{B}$ are in the noise.

We conclude from this that the magnetic field is sufficiently divergence free in our simulations to represent the magnetic forces and diffusion rates with the same accuracy as the other forces. We do not expect the code to follow all the magnetic field lines to high precision, however, because of the occasional magnetic monopole.

2.5.4. Advection test

Other tests for MHD codes were recommended by Stone et al. (1992). Figure 3 shows the results of an advection test, in which the initial conditions are: $B_x = 0$, $B_y = 1$ between grid points 100 and 150, inclusive, and $v_x = 1$, $v_y = 0$, $\rho = 1$ and $P/\rho = 10^{-10}$ everywhere. In this test, a perpendicular magnetic field bundle is advected through the grid on a current moving at supersonic speed $v_x = 1$. The test is to see how well the initially square pulse reproduces itself after moving for five times its initial width. A measure of squareness is the height of the curl $\nabla \times \mathbf{B}$, which is $(B_y[i+1] - B_y[i-1])/2$ for grid point i . Larger values of $\nabla \times \mathbf{B}$ at the ends of the pulse correspond to better advection properties.

In Evans & Hawley (1988), four different numerical schemes were tested, and they gave maximum values of $\nabla \times \mathbf{B}$ equal to 0.15, 0.18, 0.07, and 0.03. In Stone et al. (1992), three codes were tested, and they gave values of 9, 37, and 60 in their figure 2. Stone et al. used a grid spacing of 0.004 times that used by Evans & Hawley and that used here, so we multiply their $\nabla \times \mathbf{B}$ values by this factor to get the same scale. The result is then 0.036, 0.15, and 0.24 for the Stone et al. trials. Here we get a value of 0.088 for the peak in $\nabla \times \mathbf{B}$, which is intermediate between the other tests. The best results were for the piece-wise parallel

algorithm considered by Stone et al.. In the present code, the spatial derivatives are accurate only to linear order (cf. 2.2), so this accounts for the lower $\nabla \times \mathbf{B}$.

2.5.5. MHD Riemann test

Another test recommended by Stone et al. (1992) is an MHD Riemann problem with initial conditions: $P = 1$, $\rho = 1$, and $B_y = 1$ for grid position less than or equal to 400, and $P = 0.1$, $\rho = 0.125$, and $B_y = -1$ for positions 401 or larger, with $B_x = 0.75$, $v_x = v_y = 0$ everywhere. Stone et al. actually had a cell size of 0.125 and a total number of cells equal to 800, with the divider at the 400th cell, which is position 50 in his figure 4. Our cell size is 1, so we take 800 total cells with the divider at 400 in the figure. Stone et al. plotted the physical quantities at the time $t = 10$, which, with our grid, corresponds to $t = 80$ (since the speeds like P/ρ are the same, but our grid is larger by a factor of 8). Figure 4 shows the results. Each variable is in excellent agreement with the results in figure 4 of Stone et al. The numbers in the plot of density correspond to features in the solution (cf. Stone et al. 1992): (1) a fast rarefaction wave, (2) a slow compound wave, (3) a contact discontinuity, (4) a slow shock, and (5) another fast rarefaction wave.

Other tests of the basic relaxation method were shown by Jin & Zin (1995), without magnetic forces, and without the heating and cooling functions appropriate for astrophysical problems.

3. Hierarchical structure in a boundary-free turbulent region

3.1. Excitation of waves

To experiment with the origin of hierarchical structure in interstellar clouds, we ran many simulations with moderately strong Alfvén waves generated at the top and bottom of a large grid ($N_y = 800$ cells in the vertical direction plotted here, parallel to the initially uniform \mathbf{B} , and $N_x = 640$ cells in the horizontal direction). These waves traveled towards the center of the grid and interacted there, making an enhanced, irregular density structure. The boundary conditions were periodic in both vertical and horizontal directions. Thus the outgoing waves generated near the top and bottom grid edges meet and mix quickly after they cross these edges, and the inward moving waves meet after a longer time in the center of the grid.

The initial conditions of the grid are a uniform density ($\rho = 1$) and a uniform magnetic field strength ($B_y = (4\pi)^{1/2} \times 10$; $B_x = 0$), giving an Alfvén speed of $v_A = 10$, a uniform pressure $P = 1$, giving an initial sound speed $\gamma P/\rho = \gamma = 5/3$, and zero velocity in both directions. The gas is also thermally stable initially ($\Gamma = \Lambda$) and the initial cooling time is 1500 time units ($\Gamma_0 = 10^{-3}$). The magnetic diffusion rate was taken to be negligibly small, using $\omega_+ = N_y v_A / dy$, so the diffusion time would be L/v_A for a very sharp field perturbation on the scale of the grid spacing, dy , where $L = N_y dy$ is the total grid distance along the field. Simulations with more rapid diffusion are considered in section 4.

To generate waves, the velocities perpendicular to the field, v_x , at certain grid points are changed with a pattern of accelerations $\partial v_x / \partial t = Ae^{-\omega t}$ for random amplitudes A and fixed decay rates ω . The spatial positions of these accelerations are limited to within 5% and 15% of the grid size in from the ends of the grid in the direction parallel to the initial field. For a grid with $N_y = 800$ cells parallel to \mathbf{B} , the transverse accelerations occur between cells 40 and 120, and 680 and 760 in the y direction, and throughout the full width ($N_x = 640$ cells) in the perpendicular direction. The amplitudes A are taken to equal random numbers in an interval from 0 to 1 times some fixed value, chosen to give sufficiently strong

perturbations to make the desired density structures, but not so strong that the code diverges by forcing a velocity to exceed the previously assigned maximum velocity a (cf. Sect. 2.1). The decay time is taken to be $(\omega)^{-1} = N_y / (4v_A) = 20$ time units, which is the time it takes an Alfvén wave to move over 1/4 of the cells parallel to \mathbf{B} .

New accelerations are applied continuously, and the old ones terminated at the same time, so that there is always one acceleration at the bottom of the grid and another at the top of the grid. The interval between accelerations is given by a random number between 0 and 1 multiplied by the time $(8\omega)^{-1}$. The accelerations at any one time are confined to a single grid spacing in y , parallel to the field, although different accelerations can occur at different times within the intervals $(0.05 - 0.15)N_y$ and $(0.85 - 0.95)N_y$, discussed above. The accelerations are also confined to a range of grid points, Δx , perpendicular to the field (although each one may extend beyond the horizontal edges and wrap around to the other side with the periodic boundary conditions discussed above). The range Δx has a distribution of sizes comparable to the distribution of interstellar cloud radii, which is a power law $n(R)dR \propto R^{-3.3}dR$ (Elmegreen & Falgarone 1996). For the simulations, Δx varies randomly with this power law between $0.05N_x$ and $0.25N_x$.

The perturbations are designed to simulate the movements of distant clouds or other perturbations perpendicular to the magnetic field lines. These clouds presumably force whole magnetic flux tubes to move sideways in the manner simulated, since the parallel motions of clouds do not perturb the field. The cloud motions are also likely to be supersonic although generally sub-Alfvénic in space, in which case they generate strong enough waves to push matter around and influence the density, as in the simulation. As long as the waves are sub-Alfvénic, they travel relatively far from their sources (Zweibel & Josafatsson 1983) and interact to generate density structures wherever they meet. Some diffuse clouds, and much of the structure inside both diffuse clouds and the weakly self-gravitating parts of molecular clouds, can be made in this way, with remote sources of turbulent energy entering the region and moving around on magnetic field lines.

3.2. Results

Nonlinear Alfvén waves interact to form an intricate density structure. In the simulations, this structure has many scales because the initial waves have a power-law width distribution, and because, in general, non-linear terms in the MHD equations add the spatial frequencies of two mixing waves, giving an ever-increasing range of spatial frequencies.

3.2.1. Density and temperature maps

Figure 5(top) shows the density distribution of the simulation described above at a time of $t = 1024$ time units. The display measures 640×480 , with the 640-cell direction perpendicular to the initial field and representing the full grid size, and the 480-cell direction parallel to the initial field and showing only the central half of the full grid. The density increases monotonically as the color cycles from blue to yellow to red with the full rainbow, and then jumps back to blue again, followed by another cycle to red. This cyclical color display is used to emphasize hierarchical structure. There is also a density threshold ($\rho < 1.21$) below which the figure shows black. The first blue is at this $\rho = 1.21$ threshold, the second is at $\rho = 1.6$, and the highest density is red with a tiny black dot at $\rho = 1.826$, slightly to the right of the middle. Outside the plotted region, further to the top and bottom, the density gets moderately low in the “intercloud”

medium (cells 120–160, and 641–680) and then very low ($\rho = 0.19$) in the excitation region, (cells 40–120 and 680–760). The grid range for the figure is from 161 to 640 cells in the vertical direction.

The density structure in figure 5(top) is hierarchical, with clumps inside larger clumps. The “cloud” on the left has three levels in the hierarchy, making four total levels if the cloud itself is counted. The density contrast inside the cloud is not large because of numerical limitations and because of the limited range between the sonic and Alfvén speeds, and between the two equilibrium sonic speeds (both only factors of 10). The total density contrast in the whole grid is often a factor of 20 or more, but much of this occurs at the edge of the cloud where the warm intercloud medium is generated. Higher cloud and total contrasts (~ 50) were achieved in our 1D simulations (Paper I), because the grid contained 8000 cells and the waves could be driven harder. Other 2D runs with stronger wave driving made greater density contrasts, but eventually bombed when a wave velocity in the low density intercloud medium exceeded the maximum allowed by the parameter a (cf. Sect. 2.1). Larger values of a degraded the accuracy of the simulation given the grid size. Future simulations with larger grids should be able to get around these limitations by allowing larger ratios between the thermal speeds in the two phases and between the Alfvén speed and the cool thermal speed.

The density structures in figure 5 are more ellipsoidal than filamentary, and there are no obvious sharp fronts at the leading edges of the clumps. This lack of shock-like structures occurs because, even though the clumps are all moving in bulk, their speeds are less than the Alfvén speed, and also because Alfvén waves are moving through the clumps in both directions, smoothing out the sharp edges. This gives the model clumps some resemblance to real interstellar cloud clumps, but this resemblance may only be superficial because the real structures of interstellar clouds on these near-thermal scales are not generally resolved.

The complete time evolution of the density structure for this model is in Figure 6, which is an mpeg file available from the electronic version of this paper in the *Astrophysical Journal*. The mpeg file has 192 frames of size 640×480 . It is a color representation of the density evolution over a total time of 1529.2 units. Since the initial Alfvén crossing time over the entire grid (800 cells) is $800/10 = 80$, the simulation represents ~ 19 Alfvén crossing times. The thermal crossing time in the cool phase, where the sound speed is γ , is $\sim 800/\gamma \sim 480$, so the total time is 3.2 thermal crossing times (twice this if we consider only the central cloudy part, which is where the cool gas is). The color code in the mpeg file is cyclical as in figure 5, but there are three color cycles in density, with blue at $\rho = 0.3, 1.7$, and 2.0 . The maximum density is 2.3 , which is red.

The temperature structure at the same time step as in the top of figure 5 is shown in the bottom of figure 5. The highest temperatures at the top and bottom of the grid are black (threshold $P/\rho > 1.7$), and then the temperature decreases as the colors cycle from red to blue and then again from red to blue. The first red is this $P/\rho = 1.7$ level, and the second red is at $P/\rho = 1.25$. The minimum temperature, which is blue, corresponds to $P/\rho = 0.9$.

The intercloud medium at the top and the bottom of the grid is at a much higher temperature than the cloud in the middle of the grid because the density is low in the intercloud region, and then the $\Gamma - \Lambda$ function finds the high-temperature equilibrium solution. The clumps inside the cloud are slightly warmer than the interclump medium because the clumps are moving compression fronts, not stagnant clouds. This means the clumps have a continuous source of energy from their compression. The lower density and temperature in the interclump medium indicates that *the clumps are not confined by an interclump thermal pressure*, as is often proposed for interstellar clouds. Instead, the clumps are confined on their leading edges by the ram pressure from supersonic motions through the interclump medium, and they are confined on

their trailing edges by the gradient of the magnetic wave energy density that is pushing them along.

The mpeg file shows that the time evolution of the density structure is similar to what we found for 1D wave compression in Paper I: the waves push material along with them as they converge in the center of the grid, and this material builds up to make a “cloud.” The cloud has a low temperature because of its high density, given the heating and cooling functions, which have two stable thermal states. At the same time, the waves clear out the matter from the region around the cloud, leaving an intercloud medium with a low density and a high temperature equilibrium. The pressure in the cloud is higher than the initial pressure of the simulation because the incident waves push on the material they collect in the center. Nevertheless, there is total pressure equilibrium between the cloud and the intercloud medium, with the balance between kinetic, magnetic and thermal pressures changing across the cloud boundary (cf. Paper I). The 1D simulation also showed how the cloud is broken up into many smaller clouds and clumps, which have a hierarchical structure. The resolution in the 1D run of Paper I was 8000 cells, 10 times better than what we have here, so the hierarchy in density could be seen better there.

The present simulations in 2D show the same cloud formation properties and hierarchical structure as the 1D runs in Paper I. This structure changes with time as new waves enter the cloud and the existing waves continue to interact, but it always has the same hierarchical character. Three dimensional models will be necessary to fully simulate interstellar clouds, and it may be that the compression is less for a given wave amplitude in 3D than in 2D, because of the additional degree of freedom for magnetic motions in 3D. Larger compressions can always be applied to get the same level of density enhancements. The formation of hierarchical structure should not depend on the dimensionality of the simulation, however. It seems to be characteristic of non-linear wave interactions in any number of dimensions.

The mpeg file indicates that the small clumps exist for a shorter time than the large clumps. The lifetimes of clumps of various sizes are estimated to be about the sound crossing time inside the clump, regardless of scale. This lifetime is definitely larger than the internal Alfvén crossing time. This result is consistent with the view presented below in section 4 that most of the clumps are sonic or mildly supersonic features created by thermal pressure gradients parallel to the field.

3.2.2. Power Spectra

To quantify this hierarchical structure, we measured the Fourier transform of the density in directions parallel and perpendicular to the initial magnetic field over lengths of 240 cells and 640 cells, respectively (the FFT double-precision subroutine from the IBM ESSL Fortran library accommodates vectors with 640 or 240 elements). The vertical length of 240 cells was chosen to represent the inner part of the cloud; this is the central half of the vertical extent of the grid in figure 5.

For the FFT in the horizontal direction, perpendicular to the initial field, separate FFTs of the horizontal density distributions were made for each vertical grid position between cells 280 and 520, and averaged together. For the FFT in the vertical direction, separate FFTs of the vertical density distributions were made for each horizontal grid position between 0 and 640.

The results for the timestep shown in figure 5 are in figure 7, which plots the Fourier transform power, $(Re^2 + Im^2)^{1/2}$ for real and imaginary parts, Re and Im, versus the spatial frequency. The FFTs for the directions parallel and perpendicular to the field are shown on the bottom and top, respectively. The spatial frequency on the bottom figure equals 240 cells divided by the wavelength of the Fourier

component, measured in units of the grid spacing. The spatial frequency on the top equals 640 divided by the wavelength. Each plot goes from a spatial frequency of 1, which is for a wave spanning the whole extent of the corresponding direction, to 120 or 320, respectively, which are both for a wavelength of 2 cells.

The sources of excitation contribute somewhat to the FFT in the perpendicular direction. These sources have a power law size distribution between lengths of 32 and 160, which correspond to spatial frequencies of 20 and 4 in figure 7. The top diagram in that figure has a slightly shallower slope in this range than at higher frequencies. Below a spatial frequency of 20 in the perpendicular direction, the slope is ~ 2.5 ; above 20 it is ~ 3.6 , and in the parallel direction, between 10 and 100, it is ~ 3.2 .

For comparison with these model results, Green (1993), Stutzki et al. (1998), and Stanimirovic et al. (1999) found a slope of -2.8 for the power spectrum of the line-of-sight integrated intensity structure in HI and CO maps. The 2D model results are not expected to be the same as this, but the fact that both real clouds and the model results give fairly smooth power-law power spectra indicates that both have self-similar structure on a range of scales spanning at least a factor of 10.

3.2.3. Velocity Correlations

The rms velocity in a region of our simulation increases with the size of the region, as for Kolmogorov turbulence. Figure 8 shows the average rms velocities parallel and perpendicular to the initial magnetic field in squares of various sizes, as indicated by the abscissa. The time step is the same as in figure 5. The rms velocity scales as a power law with the size, S , $v_{rms} \propto S^\alpha$, with $\alpha \sim 1$ on scales smaller than ~ 30 cells, and $\alpha \sim 0.3$ on scales from 30 to 240 cells. The largest box size considered is 240, which is the vertical extent of the cloudy part of the simulation; this is much smaller than the size of the grid (800×640), so edge effects are not likely to influence this velocity correlation. Evidently, the largest scales have a velocity-size correlation similar to Kolmogorov turbulence, with a slope of about 1/3.

Smaller scales have a steeper correlation slope because the velocity differences tend to be too small on small scales. This means that the material tends to move too coherently compared to Kolmogorov turbulence on scales less than about 30 cells. The origin of this steepening could be numerical: although 30 cells should be sufficiently large to be free of resolution errors at the cellular scale, the resolution of shocks and rarefaction fronts is $\sim 5 - 20$ cells in figure 4, depending on shock strength. Also, the range of scales for driving the waves is 32 to 160, which is in the flat part of the velocity correlation.

A physical origin for the steepening at small scales is likely too, because small regions are forced to co-move by the magnetic field (Parker 1992). Indeed, the Alfvén speed is ~ 10 in the turbulence simulation, and this is much larger ($\times 100$) than the rms speed where the velocity-size correlation becomes steep in figure 8. This implies that magnetic field tension may be sufficiently strong to overpower the inertial forces from turbulence on small scales. If this is also the case in interstellar turbulence (and the 2D model results still apply in 3D), then the velocity-size correlation in molecular clouds should become steeper than the usual ~ 0.4 power law slope at linewidths less than some small fraction ($\sim 1\%$ in these simulations) of the Alfvén speed. To observe this, the total range in clump rms turbulent speeds must exceed a factor equal to the inverse of this fraction, considering that the broadest linewidth is usually the Alfvén speed.

Figure 8 also indicates that the rms velocities parallel to the magnetic field are smaller than they are perpendicular to the field. This is because the motion is forced in the perpendicular direction, and the parallel motion responds as a higher order (non-linear) effect. It may be that these two speeds are more

similar in real interstellar clouds because all of the motions there are expected to be more non-linear. There could be some decoupling between the compressive and shear waves too (Ghosh et al. 1998).

3.2.4. Summary

Interacting non-linear magnetic waves can make hierarchical, scale-free density structure with an approximately Kolmogorov velocity-size relation out of an initially uniform medium. The clouds and clumps that are produced by this mechanism are similar to what is observed in diffuse and translucent interstellar clouds, and in the parts of molecular clouds that are not strongly self-gravitating. Interstellar cloud structure is therefore likely to be partly the result of non-linear magnetic wave interactions, which is sub-Alfvénic MHD turbulence.

4. Experiments with Magnetic Damping

There have been several suggestions that stars begin to form when the minimum length for magnetic waves in the presence of ion-neutral diffusion becomes larger than a Jeans length (e.g., Mouschovias 1991). This idea is based on a model in which stars form in a more-or-less uniform cloud that is supported against self-gravity on large scales by MHD turbulence. When MHD turbulence is no longer possible, which indeed happens on sufficiently small scales in a uniform cloud, gravity wins and the local region collapses.

Our model of star formation is very different, because it proposes that clouds are never uniform. Turbulence from either inside or outside the cloud always gives them high-contrast density structure over a wide range of scales. Star formation begins when this structure melts away on scales larger than the thermal Jeans length. When there is such pervasive structure, particularly with the molecular cloud correlations between density, velocity dispersion, and size, magnetic diffusion does not become relatively more important on small scales. In fact the ratio of the diffusion time to the wave time is about constant on all scales for such a model. This is because smaller regions are denser, and so the neutral gas is more tightly bound to the ions during field line motions in just the right amount to compensate for the heightened magnetic tension (Elmegreen & Fiebig 1993). A cutoff at small scales finally arises when the density is so high that the small grains stop gyrating around the field.

The present code cannot check these ideas directly because there is no self-gravity. Instead, we assessed the importance of magnetic diffusion on cloud structure in a different way, with a series of experiments having different amounts of magnetic diffusion, adjusted through the parameter ω_+ ; this is the ion-neutral collision rate introduced in equation (34). Two runs are compared here. Both models had exactly the same parameters and random numbers in a 400×320 grid, and they had the same solutions up to the time 528.2 time units. This time equals 13.2 Alfvén wave crossing times through the vertical grid, and 1.32 sound crossing times for the cool phase, which is long enough to get a cloud in the center. Both runs also had $\omega_+ = 10^{-2} N_y v_A / dy = 40$ up to this time, but then one of them continued after this time with the same ω_+ and the other continued with $\omega_+ = 10^{-3} N_y v_A / dy = 4$. These diffusion rate constants correspond to diffusion times of $\omega_+ / (kv_A)^2$ for field gradient kB , and this time equals $\omega_0 (L/v_A) (kdy)^{-2}$, where $L = N_y dy$ is the full length of the grid along the field, $dy \equiv 1$ is the grid spacing, and $\omega_0 = 10^{-2}$ and 10^{-3} in the two cases, respectively. This means that the diffusion time is ω_0 times the product of initial Alfvén wave crossing time and the square of the scale length for magnetic field gradients, measured in grid spacings. The simulation discussed in section 3 had a large $\omega_+ = N_y v_A / dy$, which gave a diffusion time equal to the

Alfvén crossing time times the square of the scale length.

The case with rapid diffusion, $\omega_0 = 10^{-3}$, noticeably lost the perpendicular component of the field inside the cloud, which means that the wave amplitude dropped even though an external excitation with the same amplitude was still applied. The other run, with $\omega_0 = 10^{-2}$, continued with a high internal wave amplitude, following the same excitation from outside the cloud. To follow the rapid diffusion in the first case, we had to decrease the time step by a factor of 10 following this transition at $t = 528.2$; to be consistent in the second run, the timestep was decreased there too. After the transition, there were 202000 more time steps for each run, or an additional simulation time of 202 time units, which is 5 initial Alfvén wave crossing times through the whole grid.

The resulting density maps (not shown) had surprisingly little differences in the two cases – they were virtually indistinguishable, even though the wave amplitude in the case with rapid diffusion got to be 5 times less than in the other case.

We demonstrate this result in two ways. Figure 9 shows the time development of the rms density and the rms of the perpendicular component of the field, with the rapid diffusion case represented by dashed lines. These rms values are taken along the horizontal rows in the grid, perpendicular to the field. This avoids the overall gradient in the vertical direction from the general cloud structure. Thus, the rms values of the density and perpendicular field component were determined for each of the 121 horizontal rows in the middle of the grid, with each rms calculated from all 320 grid values in the horizontal rows. All these rms values were then averaged over the 121 rows to get a single rms value at each interval of 1.6 time units (every 1600 time steps). The results are plotted in figure 9. The figure shows one full cycle of the cloud’s overall density oscillation (which is still a response from the initial pulse of high pressure during cloud formation). The rms of the density is a measure of the strength of the clumpy structure; it is nearly the same in the high diffusion case as it is in the low diffusion case. The rms of the perpendicular field is a measure of the wave amplitude inside the cloud. It starts the same in the two cases, but gradually dies away in the high diffusion case, ending up about a factor of 5 weaker than in the low diffusion case. Thus *the internal magnetic waves die out, but the clumpy structure is unchanged*.

The same result is shown again in figure 10, now using Fourier transform power spectra to measure the strengths of the density and wave perturbations. These diagrams were made like figure 7, but now for a grid that is smaller in each direction by a factor 2. The two left-hand diagrams show the average power spectra of the density in the region of the cloud (120 cells parallel to the field, out of 400 total, and the full 320 cells perpendicular to the field) in the parallel-to-field direction on the bottom and perpendicular direction on the top. The two right-hand diagrams show the power spectra of the perpendicular component of the magnetic field. There are three lines in each diagram: the solid line is at the beginning of the experiment, at the time $t = 529.2$ time units, the long-dashed line is at the end of the experiment with little magnetic diffusion ($\omega_0 = 10^{-2}$), i.e., at $t = 730.2$ time units, and the short-dashed line is at the end of the experiment with a high rate of magnetic diffusion ($\omega = 10^{-3}$). Both of the top diagrams also show linear fits to the power spectra from spatial frequencies of 20 to 160, shifted upwards by factors of 100 for clarity. These linear fits reveal the similarities and differences between the power spectra without the noise.

Evidently, the density power spectra are virtually indistinguishable at the ends of the two experiments. The power spectrum of the perpendicular component of the field measured along the field (lower right diagram) is also nearly the same in the two cases; this means that the wave structure along the field is about the same with high and low diffusion. This result is not surprising because both experiments were driven with exactly the same incident waves, and both had the same wave propagation speeds through the

grid. However, the power spectrum of the perpendicular component of the field measured across the field is much less at high spatial frequency in the high diffusion case than in the low diffusion case (see the top right diagram where the short-dashed line is below the others). This means that the wave amplitude is lower after some time when the diffusion rate is high, as expected for magnetic waves in general.

What is perhaps surprising about this experiment is that even though the magnetic wave amplitude gets low after some time in the high diffusion case, the density structure is virtually unchanged. This means that enhanced magnetic diffusion does not lead to a loss of cloud structure, even when this structure is directly the result of magnetic wave interactions. How can this be?

The reason for this result is that the density structure in all of the cases considered in this paper comes from motion along the magnetic field that is driven by pressure gradients in this direction. Inside the cloud, this compression is sonic in nature, because of the dominance of the ∇P term at high density in the parallel momentum equation. This is true even when the material is pushed at supersonic (but sub-Alfvénic) speeds. The origin of the motion is the noise at the edge of the cloud, which is subject to really strong magnetic waves from outside. The waves themselves weaken and, in the high diffusion case, damp out, as they travel through the high density part of the cloud, but their damage has already been done long before this. The primary influence of the external waves is at the cloud edge, where the magnetic energy and the momentum of interclump motions get converted into cloud density pulses, like puffs of wind, that travel through and interact with each other in the interior of the cloud. Even when the internal magnetic wave energy is damped, these sonic pulses still make essentially the same density structures inside the cloud.

If the density structure inside real interstellar clouds is the result of interacting, non-linear magnetic waves, as in the models discussed here, then this structure would seem to be relatively unaffected by an enhancement in magnetic diffusion that might result from an increase in density or an excess shielding of external radiation. This result suggests that enhanced magnetic diffusion is not the key to the onset of star formation in weakly self-gravitating clouds. Of course, magnetic diffusion can still play a very important role later, during the accretion phase inside a strongly self-gravitating cloud piece, but this process is not simulated here.

5. Experiments with Gravitational Density Gradients

In a model where clouds and clumps form by interacting non-linear magnetic waves, the only way the tiny structure can disappear as a necessary precursor to star formation is if both the magnetic waves and the sonic pulses they create damp out before they reach the cloud center. The previous section showed that even when the waves damped out, the sonic pulses that were generated in the intercloud medium and at the cloud edge still remained.

Here we consider a different way to damp the sources of internal cloud structure. This occurs when both the external waves and the sonic pulses have to climb up a steep density gradient before getting to the center. The increased density removes the wave and pulse kinetic energy by momentum conservation, and this leaves the center with relatively little turbulence to drive structure formation. Such a cloud density gradient occurs naturally when the cloud becomes significantly self-gravitating. This means that *the gradual contraction of a cloud under the influence of self-gravity should be enough to exclude externally generated turbulence and initiate the decay of tiny cloud structure in the core*.

This effect is demonstrated in two ways. First WKB solutions to the wave equation are given for waves

traveling through a region with a centralized density enhancement. These analytical solutions show the expected decrease in wave amplitude in the cloud center. Second, two numerical experiments are run on 800×640 grids that have a fixed, plane-parallel gravitational force in the direction along the field, which gives them a $\rho = \csc^2[(y - y_0)/H]$ general density structure underneath the wave structure. These two experiments have different scale heights, H , and when combined with the simulation discussed in Section 3, show a gradual loss of density structure as the scale height decreases and the central density increases.

5.1. WKB Solutions to waves in density gradients

We consider here a simple wave of any kind that satisfies the wave equation

$$\frac{\partial^2 W}{\partial t^2} = a^2 \frac{\partial^2 W}{\partial y^2} \quad (62)$$

for wave amplitude W and wave speed $a(y)$ that is a function of position, y . Using the WKB approximation for weak waves, we write

$$W(y, t) = e^{i\omega t - i \int_{-\infty}^y k dy} \quad (63)$$

for frequency ω , wavenumber $k = 2\pi/\lambda$ and wavelength λ . Substituting this waveform into the wave equation gives a differential equation for $k(y)$:

$$\frac{\omega^2}{a^2} = ik' + k^2 \quad (64)$$

for derivative $k' = dk/dy$. Substituting the real and imaginary components for complex $k = k_r + ik_i$ then gives two equations, one real and the other imaginary. We look for pure wave solutions with real ω , and this allows us to eliminate one equation, giving as a result a single equation for the real component of k :

$$k_r'' - \frac{3(k_r')^2}{2k_r} + 2k_r^3 - \left(\frac{\omega^2}{a^2}\right) 2k_r = 0. \quad (65)$$

The imaginary component of k was eliminated from the above equation, but is given by $k_i = -k_r'/2k_r$.

Equation 65 was solved numerically for $k_r(y)$. The wave speed is taken to be

$$a(y) = \frac{e^{y/H} + e^{-y/H}}{e^{y_e/H} + e^{-y_e/H}}, \quad (66)$$

so it equals unity at the edge of the numerical grid, where $y \equiv \pm y_e = 5$, and there is a gradual slow down of the wave to a minimum wave speed of $2/(e^{y_e/H} + e^{-y_e/H})$ at $y = 0$. In the cloud model, this slow down is the result of an increased density. The desired result is the ratio of the wave amplitude at the center to the incident wave amplitude at the edge. The boundary condition for the integration is $k_r = \omega/a$ at $y = -y_e$.

Figure 11 shows the result. The average wave amplitude inside the central scale height of the grid, between $y = \pm H$, is shown as a function of the central wave speed. The wave amplitude decreases as the central wave speed decreases, almost exactly as the square root for this model; i.e., $\langle W \rangle \approx a(0)^{1/2}$.

This decrease in amplitude with increasing density is essentially the result of gradual wave reflection at the cloud edge. The net flux toward the cloud on each side is the difference between the incident and reflected wave fluxes, and by conservation, must equal the respective fluxes in the same directions inside the cloud. We checked the WKB result by considering a cloud/intercloud boundary with a sharp

immovable edge and a hard barrier inside the cloud to simulate reflection symmetry through the cloud (this is analogous to our MHD solution, which has waves incident from both sides of the cloud). We calculated the reflection and transmission amplitudes of the waves, and then averaged the internal and external wave energy densities over a factor of 100 in wavenumber (to smooth out resonances). We found again that the average wave amplitude inside and outside the cloud is always proportional to the square root of the local Alfvén speed.

This result differs from the proposal by Xie (1995) that Alfvén waves maintain an amplitude inversely proportional to the square root of density. In our case, the total field strength is about constant and the wave amplitude varies as the inverse fourth root of density. This implies that the wave pressure and energy density are lower inside the cloud than outside, demonstrating the effect of shielding. There is also a net compression of the cloud from this shielding, rather than a wave-pressure equilibrium inside and outside the cloud, as there would be in the case considered by Xie.

5.2. MHD solutions to waves in density gradients

The same problem was studied with the MHD code. We ran two more 2D simulations as in section 3 but with an additional acceleration from constant gravity, directed toward the center of the grid in the vertical direction, along the field. The gravitational acceleration, g , was written as part of the equation of motion in equation 35. Here it given by

$$g(y) = -\left(\frac{2a_0^2}{H}\right)\left(\frac{e^{(y-y_0)/H} - e^{-(y-y_0)/H}}{e^{(y-y_0)/H} + e^{-(y-y_0)/H}}\right), \quad (67)$$

for initial isothermal speed a_0 given by $P/\rho = a_0^2 = 1$. The corresponding initial condition for density was taken to be the equilibrium value

$$\rho(y) = \left(\frac{e^{-y_0/H} + e^{y_0/H}}{e^{(y-y_0)/H} + e^{-(y-y_0)/H}}\right)^2. \quad (68)$$

The midpoint of the grid in the vertical direction is $y_0 = 400$. This density is normalized to equal 1 at the top and bottom edge of the grid ($y = 2y_0$ and 0, respectively), as in section 3, but now the density is higher in the center by a factor that depends on the scale height. We chose one run with $H = 300$ cells, giving a central density enhancement of 4.1, and another with $H = 235$, giving a central density of 8.0.

The simulations were run for as long as that in section 3, with the same random numbers and external wave stimulations. This allowed time for internal adjustments and large-scale cloud oscillations. The results show that the transverse wave velocity inside the cloud, and the level of density fluctuations, both decrease as the central density from gravity increases. Figure 12 shows the power spectra of the density at the bottom and the transverse velocity at the top for the three runs indicated by different line types. These power spectra were taken from Fourier transforms in the transverse direction, as on the top of figure 7. The density power spectra are normalized to the power at zero spatial frequency to remove the differences between the absolute densities in the clouds in these cases (recall that the central density is ~ 2.5 in the gravity-free case, while it is ~ 4 and ~ 8 in the two gravity cases). The sloping lines in the figures are least squares fits to the power spectra between frequencies 20 and 320, shifted upwards by factors of 100 for clarity. The fits indicate more clearly than the noisy power spectra that the gravity-free case, indicated by the solid line, has more power in both transverse wave velocity and density structure than the two centrally condensed cases.

The downward shift in the velocity power spectrum when gravity is added is a factor of 2.1 for the case with a central density of 4 and 3.1 for the case with a central density of 8, measured at a spatial frequency of 20. These numbers compare well with the results in figure 11, considering that the minimum wave speed is proportional to the inverse square root of the density. The downward shifts in the density power spectra at a frequency of 20 are factors of 3.0 and 3.7, respectively. The degradation in density structure is greater than in velocity structure, as expected for density caused by compression. If the wave energy density completely dominated the thermal pressure, then the density variations would scale as the square of the velocity variations.

The power spectra of velocity and density in the direction parallel to the field do not change much when the cloud becomes centrally condensed. This is analogous to what was found for the magnetic diffusion tests, where only the perpendicular direction had any change in magnetic wave amplitude. This is the result of a similar wave structure parallel to the field in all the cases of central condensation, following from the same wave stimuli. The primary differences between the runs are in the wave amplitudes.

These results indicate that *the internal velocity and clumpy structure begins to disappear as the overall cloud gets more and more centrally condensed from gravity.*

6. Conclusions

The Jin & Xin (1995) relaxation algorithm has been adapted to do MHD simulations with an energy equation and magnetic diffusion term relevant to astrophysical problems. The code tested well in comparison with other astrophysical MHD codes, and was judged to be adequate for the problems considered here.

MHD simulations in two dimensions were run for several cases to address the question of how hierarchical and scale-free clumpy structure inside interstellar clouds and in the general interstellar medium might be created, and how this structure might be induced to go away on very small scales as a precursor to star formation.

The simulations in section 3 showed that interacting non-linear Alfvén waves can make a whole 2D cloud and self-similar clumpy structure inside of it. This structure was demonstrated by its power-law power spectrum and by its overall hierarchical appearance. The clumps were rounded rather than filamentary, with no obvious shock structures, and each one existed for about one internal sound crossing time, regardless of scale. The thermal pressure of the interclump medium does not confine the clumps. They owe their existence entirely to kinematic pressures that are associated with their motions and with the relative motions of the surrounding gas. The overall structure had a realistic Kolmogorov velocity-separation relation at large scales, but it had a steeper relation at small scales for unknown reasons.

The simulations in section 4 showed that enhanced magnetic diffusion caused the Alfvén wave amplitude to decrease inside the cloud, but it did not change either the amplitude or the pattern of the density structure. This experiment suggests that, on interstellar scales which span the range between subthermal and superthermal motions, the density structure comes primarily from strong sonic pulses that move along the field and interact in complex ways. Changes in the magnetic diffusion rate do not change these density structures as long as the sonic pulses that drive them continue to have a source.

The simulations in section 5 showed that both the internal waves and the small-scale density structures they help create go away when the overall cloud has a density gradient, as might result from bulk self-gravity. This is because externally generated waves have trouble penetrating a cloud and making small

scale structure by non-linear interactions when they have to climb a strong density gradient first. A WKB solution to the wave equation obtained the same result.

We view the processes acting in these simulations to be at the bottom end of the range of scales of interstellar cloud structures, near the thermal pressure limit where turbulent pressures are only slightly larger than thermal. We believe that a larger computational grid would show a more extended hierarchical structure on larger scales, but the same wave interaction processes on small scales. Most observations of real interstellar clouds cannot yet resolve the small scales that are simulated here, but only the larger parts of the hierarchy of cloud structure. This implies that if the models are a guide to reality, then the supersonic turbulence that is observed in interstellar clouds is not really supersonic at the atomic level, but nearly thermal locally, i.e., with relatively small local velocity gradients and few strong shocks. In that case, the appearance of supersonic motions is the result of a superposition of locally near-thermal motions on a wide range of unresolved scales, with a Kolmogorov-type velocity-size correlation generating the largest speeds.

The simulations also suggest a mechanism for star formation that is relevant to the modern model of interstellar clouds, in which many clouds and the clumpy structures inside them come from magnetic turbulence and the associated non-linear wave interactions, and in which these structures initially extend down to very small scales, far past the scale of the minimum stellar mass. Star formation in such a cloud model does not require any fragmentation mechanism, nor any other mechanism that separates out stellar mass units from the background, because these clouds are always highly fragmented anyway, on all scales, including the range covered by stars. That is, stellar mass fragments are in all clouds all the time, as a result of turbulence. Star formation with such a cloud model requires a smoothing mechanism instead, one in which sub-stellar fragments coalesce and meld together to build up smooth pools with stellar masses, without the destructive and dividing influence of turbulence inside and around this pool.

The simulations suggest that enhanced magnetic diffusion is probably not important for this first step in star formation, but the formation of a gradual density gradient from bulk self-gravity is. This result leads to the following scenario for star formation:

Star formation begins in a region of interstellar gas when various processes render it so massive that gravitationally driven motions become comparable to the externally and internally driven turbulent motions. At this time, the cloud begins to contract under its own weight and builds up a density gradient. Such a density gradient will shield the cloud from turbulence in the outside world, and lead to a reduction in the internal turbulent energy, as well as a loss of internal small-scale structure. Because the smallest scales evolve the quickest, this loss of structure will begin on the smallest scales and quickly increase the mass of the smallest smooth, thermally-dominated clumps. When these smallest, thermally-dominated masses increase to the point where gravitationally driven motions inside of them begin to dominate thermal motions, they collapse catastrophically to make one or a few stars each in dense cores. Neighboring clumps do the same, all rather quickly on the scale of the overall cloud evolution, forming a hierarchical arrangement of stars and star clusters on time scales comparable to the turbulent crossing times for those scales. If the self-gravity of the overall cloud is very strong, then this resulting cluster will be very dense, if not, then only a sparse cluster will form. This is in agreement with the densities, structures and formation times of real star clusters (see review in Elmegreen et al. 1999).

At the present time, these initial star-formation processes are beyond the limit of angular resolution in general cloud surveys. They also should occur quickly on the first substellar scales, making the initial smoothing process unlikely to see. This implies that interstellar clouds with and without star formation may look very similar on today's observable scales, and their difference only show up when the angular

resolution is great enough to see structures at ~ 500 pc with far less than a stellar mass. Our prediction is that star-forming clouds will have much less structure on sub-stellar scales than pre- or non-star forming clouds, and that extremely young star-forming regions will have a relative number of substellar clumps that is midway between those of the non- and the active star-forming clouds. That is, the clump mass spectrum will change from a power law to very small scales in non-star-forming clouds to one with a flattened or turned-over distribution function at low mass in pre- or active star-forming clouds, and the mass at this flattening or turnover will increase up to the minimum stellar mass as the cloud becomes more and more active with star formation. Another signature of this process is the hierarchical structure of young stellar positions, whatever the scale and density of star formation, and the appearance of clusters rather quickly, in about a local crossing time.

Acknowledgements: Helpful comments on the manuscript by Dr. A. Lazarian and S. Shore are appreciated.

REFERENCES

Bania T.M. & Lyon J.G. 1980, *ApJ*, 239, 173
Ballesteros-Paredes, J., Vázquez-Semadeni, E., & Scalo, J. 1999, *ApJ*, in press
Bertoldi, F., & McKee, C. 1992, *ApJ*, 395, 140
Brand, P.W.J.L., & Zealey, W.J. 1975, *A&A*, 38, 363
Cox, D.P., & Smith, B.W. 1974, *ApJ*, 189, L105
Dai, W., & Woodward, P.R. 1998, *ApJ*, 494, 317
Dickman, R.L 1985, in *Protostars and Planets II*, eds. D. C. Black & M.S. Matthews, Tucson: University of Arizona, p. 150
Elmegreen, B.G. 1979, *ApJ*, 231, 372
Elmegreen, B.G. 1989, *ApJ*, 342, L67
Elmegreen, B.G. 1990, *ApJ*, 361, L77
Elmegreen, B.G. 1991, in *Physics of Star Formation and Early Stellar Evolution*, ed. C.J. Lada and N. Kylafis, Dordrecht: Kluwer Academic Publishers, p. 35
Elmegreen, B.G. 1993a, in *Protostars and Planets III*, eds. E. H. Levy and J. I. Lunine, Tucson: Univ. Arizona, p. 97
Elmegreen, B.G. 1993b, *ApJ*, 419, L29
Elmegreen, B.G. 1996, in *Unsolved Problems of the Milky Way*, ed. L. Blitz and P. Teuben, Dordrecht: Kluwer, p. 551
Elmegreen, B.G. 1997a, *ApJ*, 477, 196
Elmegreen, B.G. 1997b, *ApJ*, 480, 674 (Paper I)
Elmegreen, B.G. 1998, in *Origins*, ed. C.E. Woodward, J.M. Shull, and H.A. Thronson, San Francisco, ASP Conf.Ser., 148, 150
Elmegreen, B.G. 1999, *ApJ*, 515, April 10, in press
Elmegreen, B.G., & Fiebig, D. 1993, *A&A*, 270, 397

Elmegreen, B.G. & Falgarone, E. 1996, ApJ, 471, 816

Evans, C.R., & Hawley, J.F. 1988, ApJ, 332, 659

Falgarone, E. 1989, in Structure and Dynamics of the Interstellar Medium, ed. Tenorio-Tagle, G. Moles, M., & Melnick, J., Berlin: Springer, p.68.

Falgarone, E., & Phillips, T. 1990, ApJ, 359, 399

Falgarone, E., Phillips, T., & Walker, C.K. 1991, ApJ, 378, 186

Falgarone, E., Puget, J.L., & Pérault, M. 1992, A&A, 257, 715

Falgarone, E., Panis, J.-F., Heithausen, A., Perault, M., Stutzki, J., Puget, J.-L., & Bensch, F. 1998, A&A, 331, 669

Field, G.B., Goldsmith, D.W., & Habing, H.J. 1969, ApJ, 155, L149

Field, G.B., & Saslaw, W.C. 1965, ApJ, 142, 568

Gammie, C.F. & Ostriker, E.C. 1996, ApJ, 466, 814

Ghosh, S., Matthaeus, W.H., Roberts, D.A., & Goldstein, M.L. 1998, J. Geophys.Res., 103, 23705

Goldreich, P., & Lynden-Bell, D. 1965, MNRAS, 130, 97

Goldreich, P., & Sridhar, S. 1995, ApJ, 438, 763

Green, D.A. 1993, MNRAS, 262, 327

Hartmann, L., Ballesteros-Paredes, J., & Vazquez-Semadeni, E. 1998, BAAS, 193, 7203

Hills, J.G. 1972, A&A, 17, 155

Hunter, J.H., Jr., & Fleck, R.C. 1982, ApJ, 256, 505

Jin, S. 1995, J. Comp. Phys., 122, 51

Jin, S., & Xin, Z. 1995, Comm. Pure and Applied Math, 48, 235

Klein, R.I., McKee, C.F., & Colella, P., 1994 ApJ, 420, 213

Kwan, J. 1979, ApJ, 229, 567

LaRosa, T.N., Shore, S.N., & Magnani, L. 1999, ApJ, 512, 761

Larson, R.B. 1981, MNRAS, 194, 809

Lazarian, A. 1995, A&A, 293, 507

Lazarian, A., & Pogosyan, D. 1999, in press

Low, F.J., et al. 1984, ApJ, 278, L19

Magnani, L., Blitz, L., & Mundy, L. 1985, ApJ, 295, 402

Mandelbrot, B.B. 1983, The Fractal Geometry of Nature, San Francisco: Freeman

MacLow, M.-M., McKee, C.F., Klein, R.I., Stone, J.M., & Norman, M.L. 1994, ApJ, 433, 757

MacLow, M.-M., Klessen, R. S., Burkert, A., & Smith, M. D. 1998, Phys. Rev. Lett., 80, 2754

McKee, C.F. & Ostriker, J.P. 1977, ApJ, 218, 148

Mouschovias, T.C. 1991, ApJ, 373, 169

Myers, P.C. 1998, ApJ, 496, L109

Myers, P.C., & Lazarian, A. 1998, ApJ, 507, L157

Nordlund, A., & Padoan, P. 1998, in Interstellar Turbulence, Proceedings of the 2nd Guillermo Haro Conference, eds: J. Franco, J. & A. Carraminana, Cambridge: Cambridge Univ., p. 62

Padoan, P. 1995, MNRAS, 277, 377

Padoan, P. 1998, in Interstellar Turbulence, Proceedings of the 2nd Guillermo Haro Conference, eds: J. Franco, & A. Carraminana, Cambridge: Cambridge University, p. 64.

Passot, T., Vazquez-Semadeni, E., & Pouquet, A. 1995, ApJ, 455, 536

Parker, E.N. 1966, ApJ, 145, 811

Parker, E.N. 1992, ApJ, 401, 137

Sasao, T. 1973, PASJ, 25, 1

Salpeter, E.E. 1976, ApJ, 229, 533

Scalo, J. 1985 in Protostars and Planets II, ed. D.C. Black & M.S. Mathews (Tucson: Univ. of Arizona Press), 201

Scalo, J. 1987, In Interstellar Processes, eds. D.J. Hollenbach and H.A. Thronson Jr., Dordrecht: Reidel, p. 439.

Scalo, J. 1990, In Physical Processes in Fragmentation and Star Formation, eds. R. Capuzzo-Dolcetta, C. Chiosi, and A. Di Fazio, Dordrecht: Kluwer, p. 151.

Scalo, J.M., Vazquez-Semadeni, E., Chappell, D., & Passot, T. 1998, ApJ, 504, 835

Spangler, S.R. 1998, in Interstellar Turbulence, eds. J. Franco, & A. Carraminana, Cambridge: Cambridge University Press, p. 36

Sreenivasan, K. R. 1991, Ann.Rev.Fluid Mech., 23, 539

Stanimirovic, S., Staveley-Smith, L., Dickey, J.M., Sault, R.J., & Snowden, S.L. 1999, MNRAS, 302, 417

Stone, J.M., & Norman, M.L. 1992, ApJS, 80, 971

Stone, J.M., Hawley, J.F., Evans, C.R., & Norman, M.L. 1992, ApJ, 388, 415

Stone, J.M., Ostriker, E.C., & Gammie, C.F. 1998, ApJ, 508, 99

Struck-Marcell, C., & Scalo, J.M. 1984, ApJ, 277, 132

Stutzki, J., Genzel, R., Graf, U., Harris, A., Sternberg, A., and Gusten, R. 1991, in Fragmentation of Molecular Clouds and Star Formation, ed. E. Falgarone, F. Boulanger, and G. Duvert, Dordrecht: Kluwer, p. 235.

Stutzki, J., Bensch, F., Heithausen, A., Ossenkopf, V., and Zielinsky, M. 1998, A&A, 336, 697

Tenorio-Tagle, G., & Bodenheimer, P. 1988, ARAA, 26, 146

Tomisaka, K. 1987, PASJ, 39, 109

van Leer, B. 1979, J. Comp. Physics, 32, 101

Vazquez-Semadeni, E. 1994 ApJ, 423, 681

Vazquez-Semadeni, E., Passot, T., & Pouquet, A. 1995, ApJ, 441, 702

Vazquez-Semadeni, E., Passot, T., & Pouquet, A. 1996, ApJ, 473, 881

Vazquez-Semadeni, E., Ballesteros-Paredes, J. & Rodriguez, L.F. 1997, ApJ, 474, 292

von Weizsacker, C.F. 1951, ApJ, 114, 165

Xie, T. 1997, ApJ, 475, L139
Xu, J. & Stone, J.M. 1995, ApJ, 454, 172
Yue, Z.Y., Zhang, B., Winnewisser, G., & Stutzki, J. 1993, Ann Physiks, 2, 9
Zweibel, E.G., & Josafatsson, K. 1983, ApJ, 270, 511

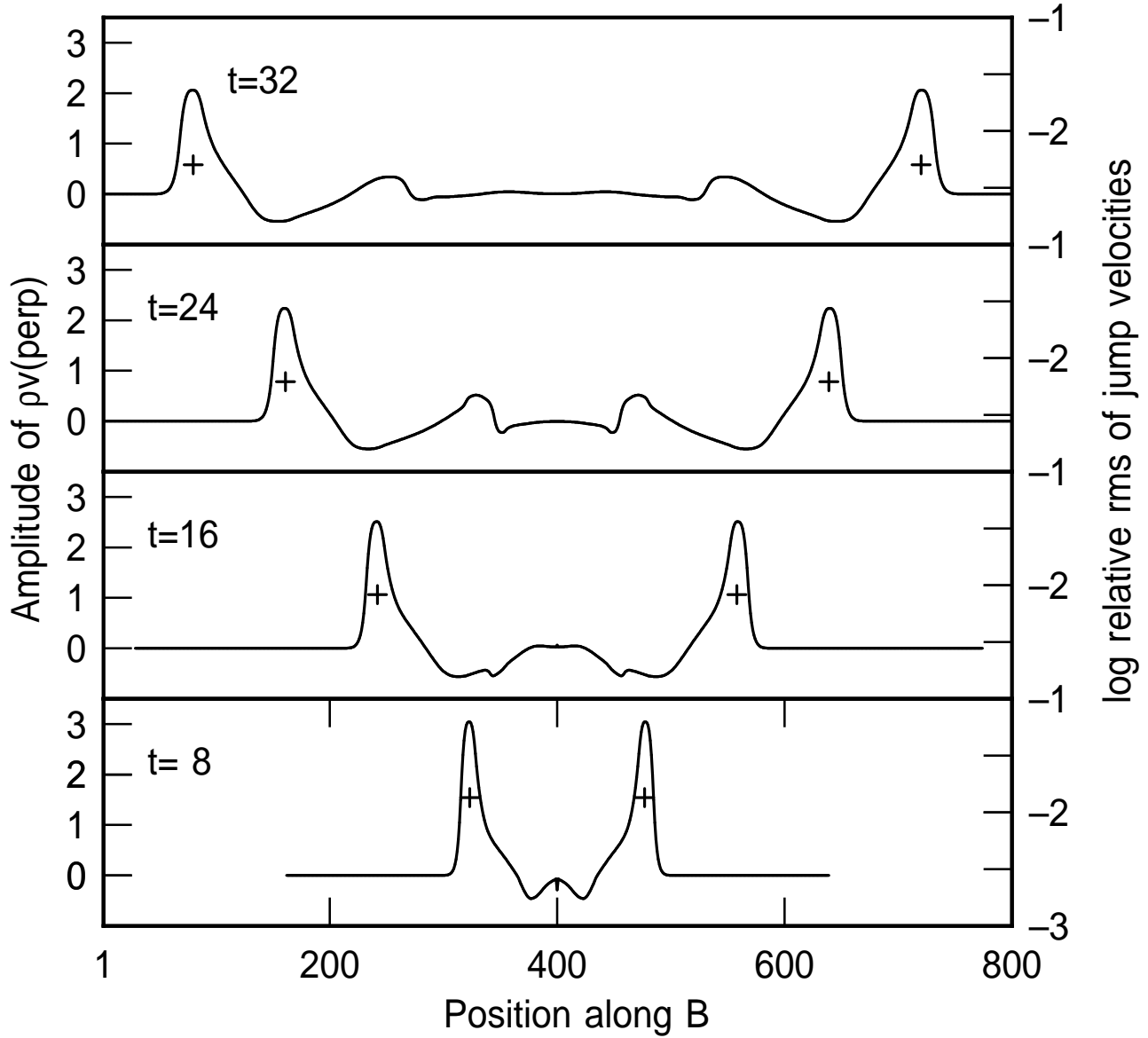


Fig. 1.— The perpendicular momentum flux, ρv_x , is shown as a function of position along the magnetic field for four time steps following a time-sinusoidal perturbation in the center. The left-hand axis shows the amplitude of the momentum. The perturbation drives waves outward, and these waves steepen and push matter along with them, slowing and weakening as they go. The relative rms deviations between the four measures of the shock speed, from the four jump conditions, are shown by plus signs at the grid points where the density peaks, using the right-hand axes to indicate the amplitude. The rms deviation is typically around 1%.

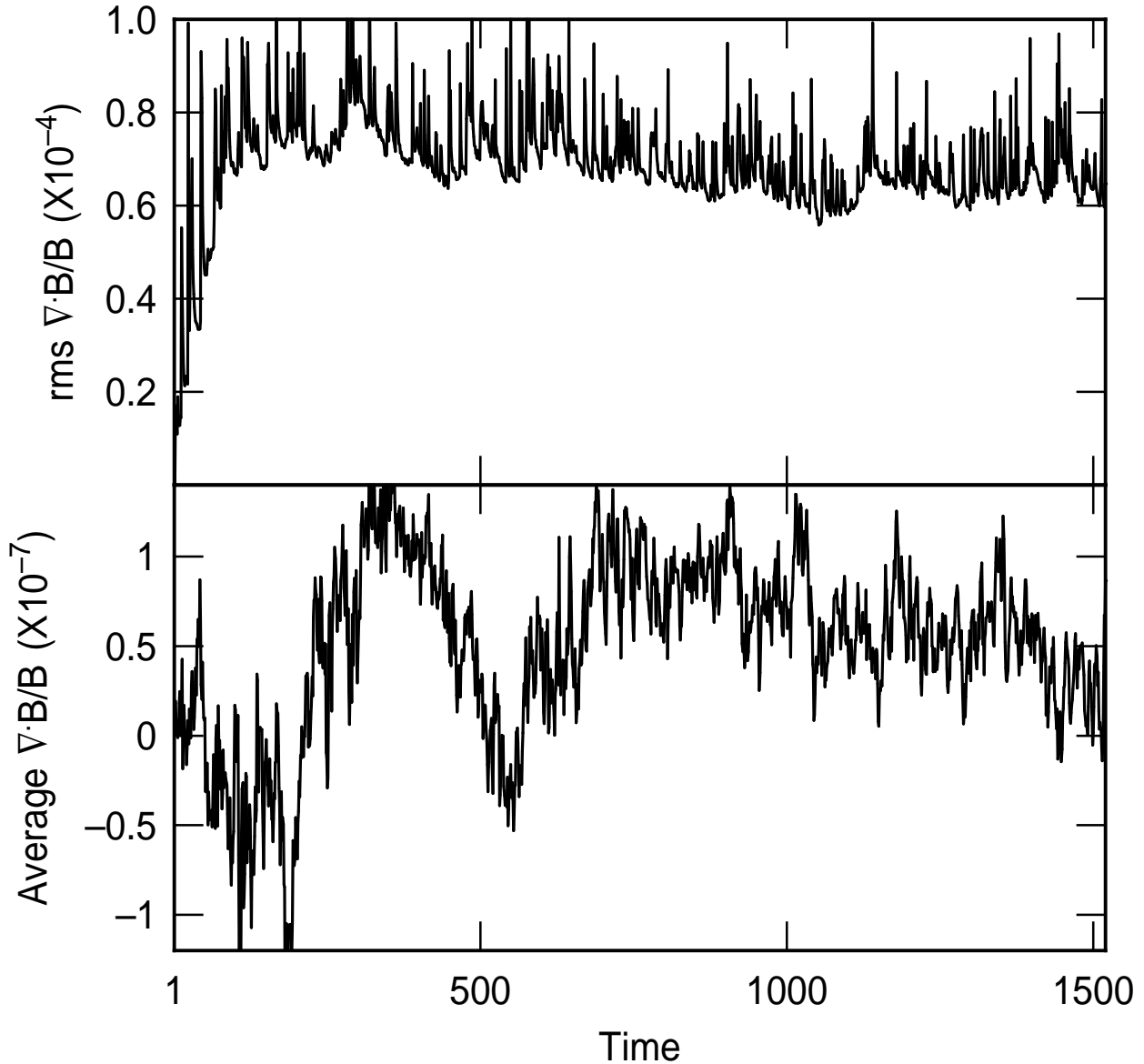


Fig. 2.— The average and rms values of the quantity $\nabla \cdot \mathbf{B} / (\mathbf{B} \cdot \mathbf{B})^{1/2}$ are shown as functions of dimensionless time, with one plotted point per time unit, which is 100 computational time steps.

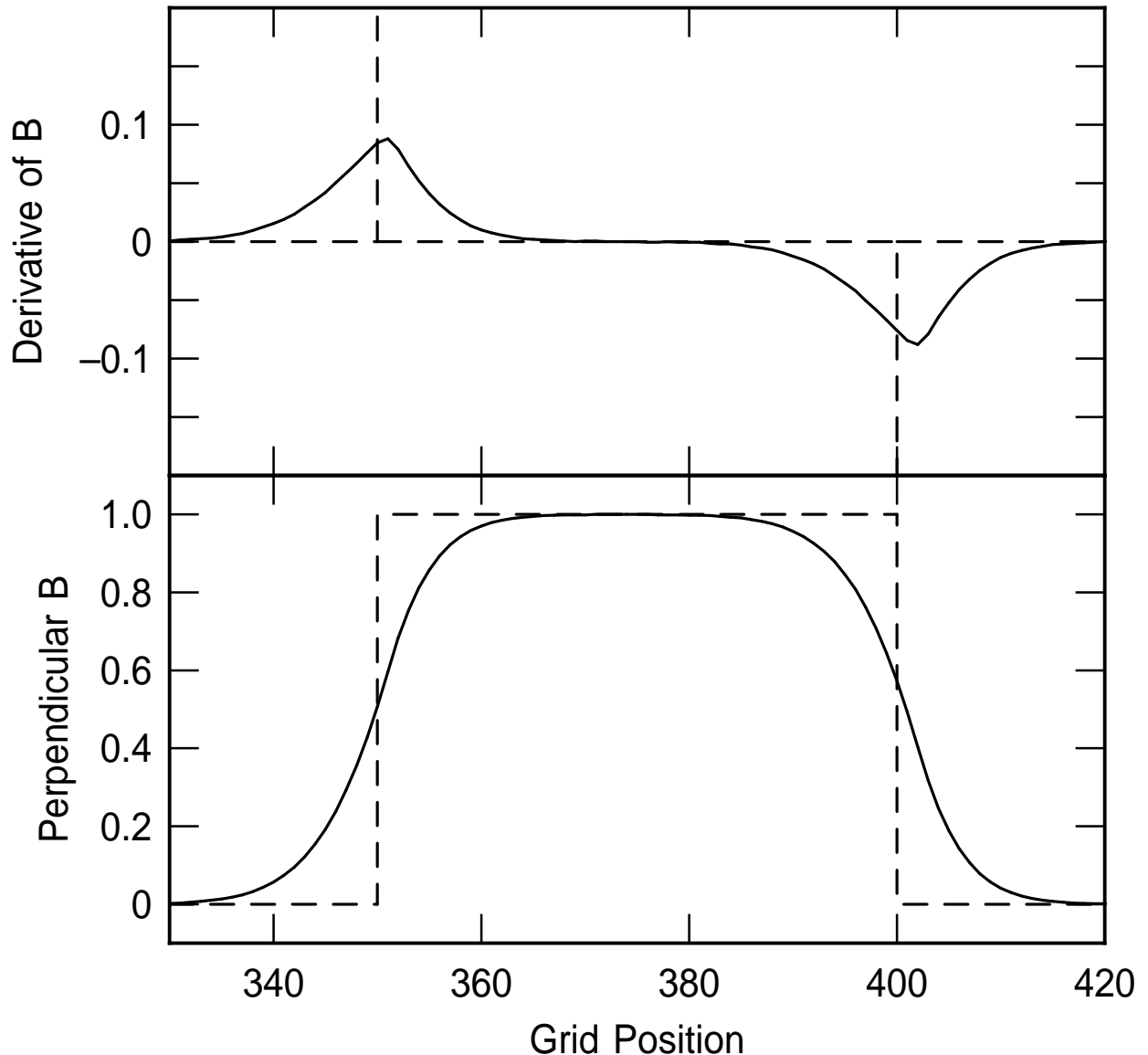


Fig. 3.— (bottom) The perpendicular magnetic field strength versus the grid position is shown for an initially square magnetic pulse that has been advected along with a velocity flow field for a distance of five times its initial thickness. (top) The curl of the field for this pulse, giving a measure of the sharpness of the edges.

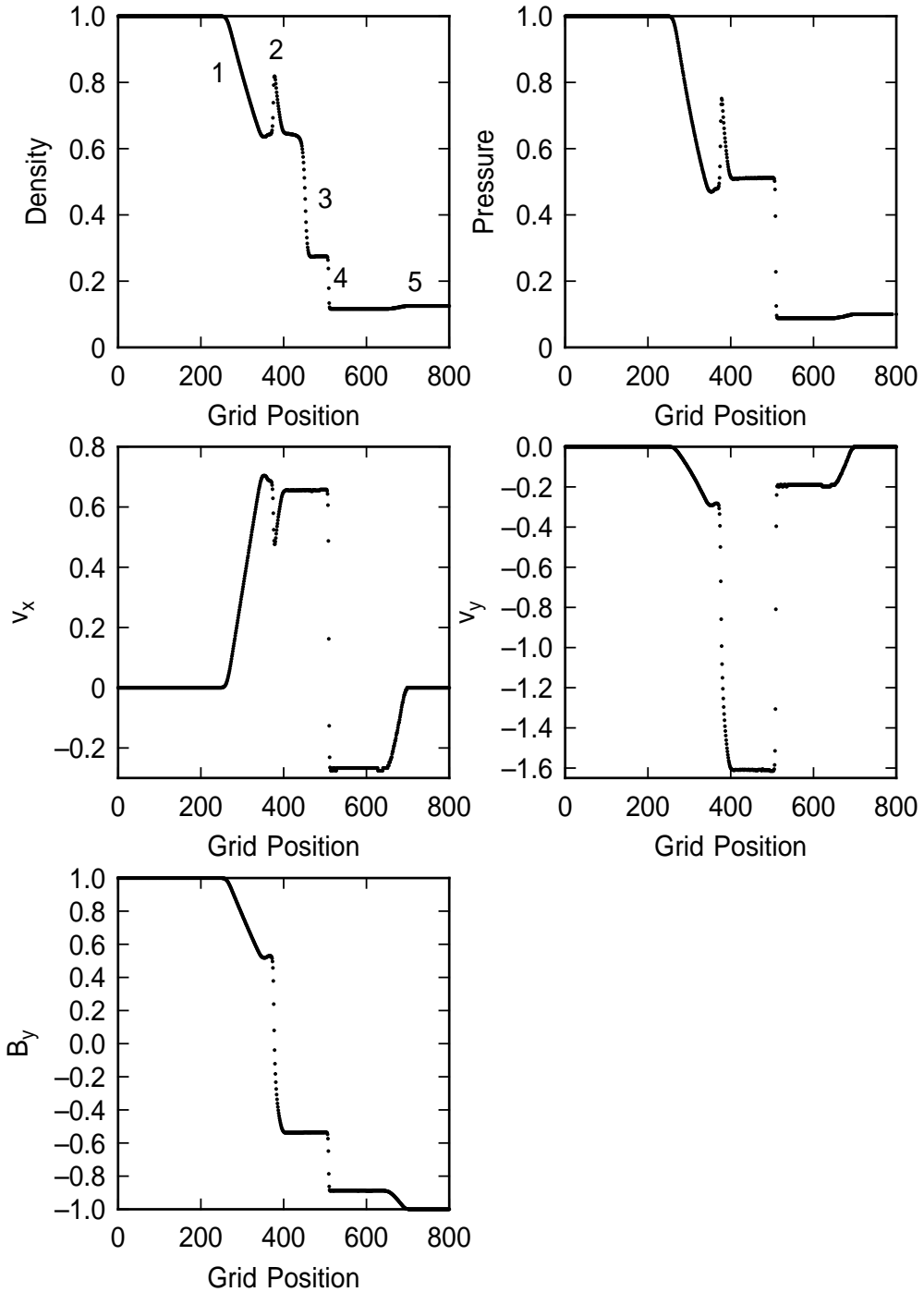


Fig. 4.— Physical variables in the MHD Riemann test discussed by Stone et al. (1992). The test here matches well the results in Stone et al.. The five main features in these figures are (1) a fast rarefaction wave (2) a slow compound wave, (3) a contact discontinuity, (4) a slow shock, and (5) another fast rarefaction wave.

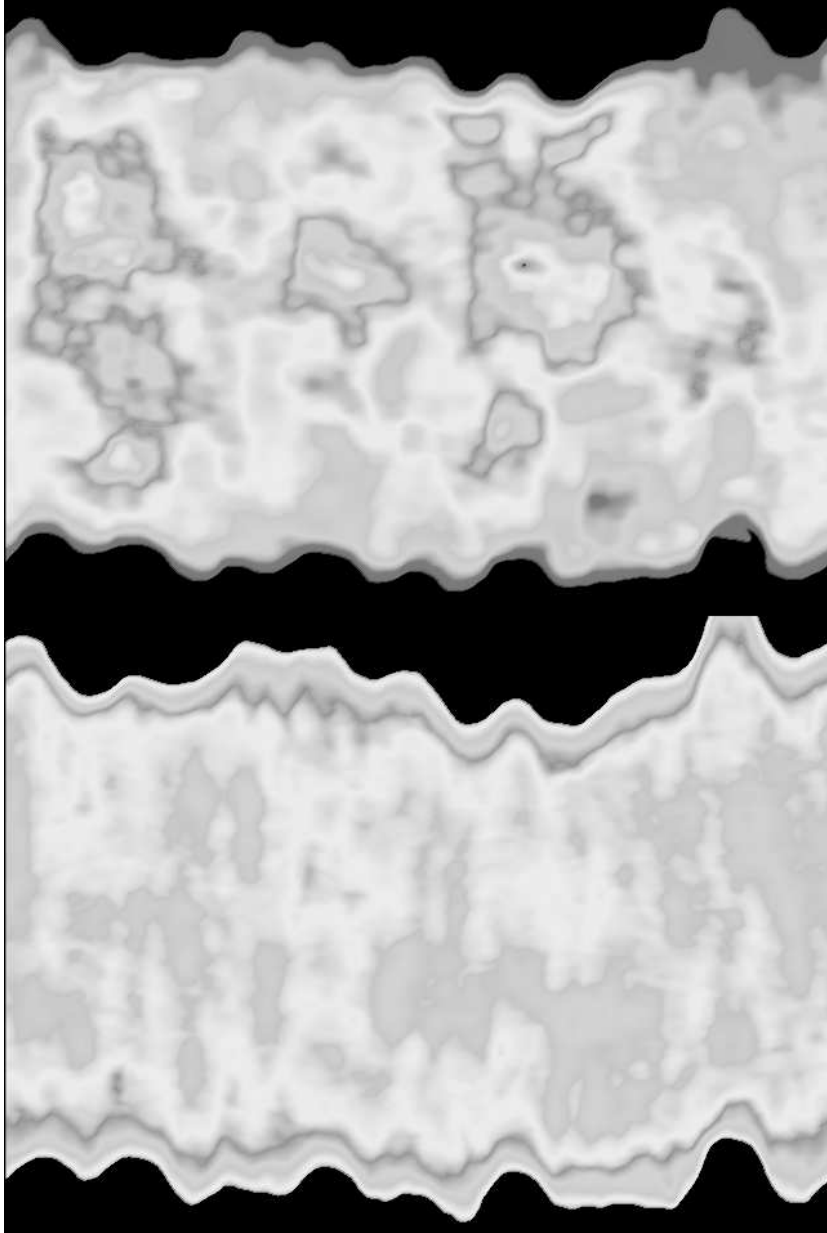


Fig. 5.— (top) The density structure in an 800×640 simulation, showing the inner 480×640 rectangle. The initial magnetic field is vertical and the excitation zones are off the picture, to the top and bottom of the grid. The density is color coded to emphasize the hierarchical structure, with two cycles of color going from blue to red as the density increases. The peak density is 1.826, the black level at the edge is 1.23, and the minimum density at this time step, which occurs outside the rectangle shown, is 0.19. (bottom) The corresponding temperature structure, with red hotter than blue, in two cycles. The clumps are warmer than the interclump medium, indicating that the clumps are not confined by thermal pressure from the interclump medium, but by the kinematic pressure from their motion through this interclump medium. NOTE: gray only for astro-ph.

Fig. 6.— MPEG movie of the 800×640 simulation shown in figure 5, with density color coded in three cycles from blue to red, with blue at densities of 0.3, 1.7, and 2.0.

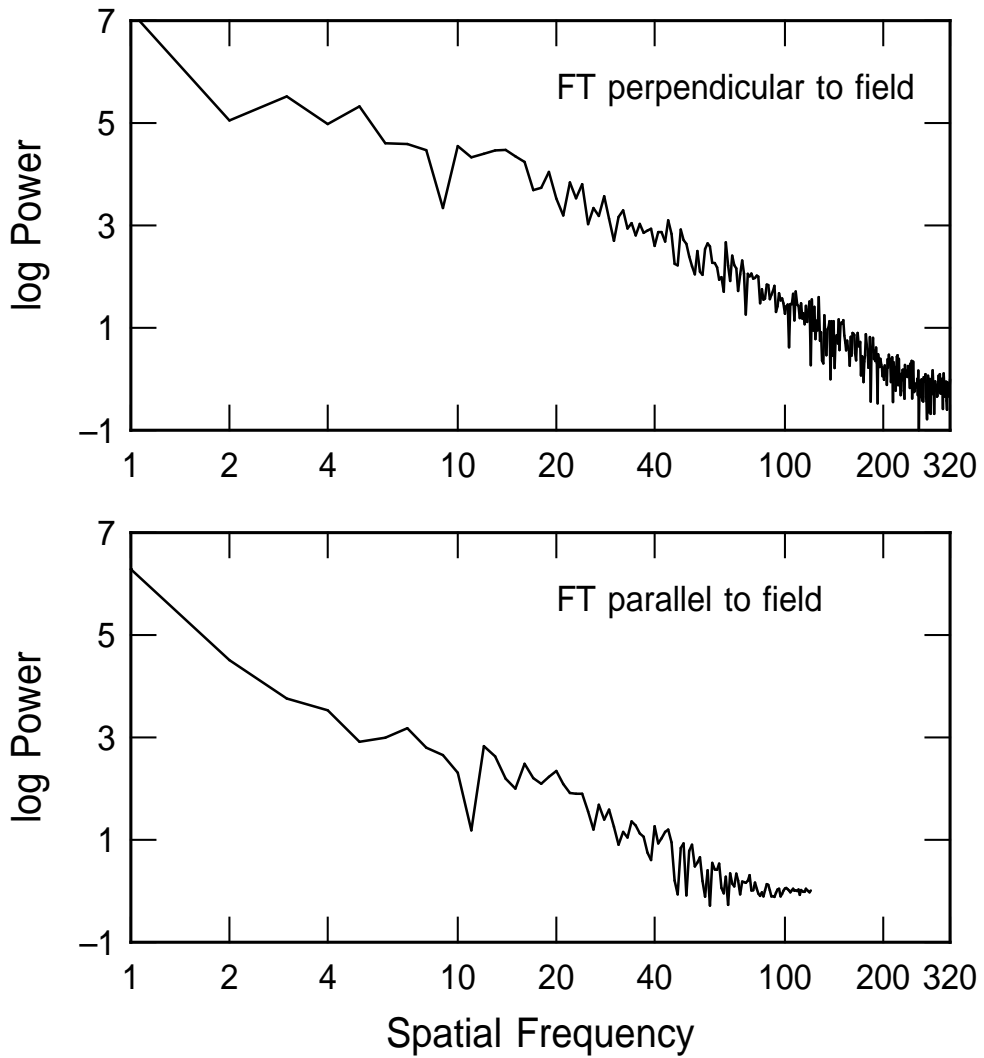


Fig. 7.— Power spectra of the density structure for the model shown in figure 5. The average power spectrum for the direction parallel to the field is shown at the bottom, and for the direction perpendicular to the field at the top.

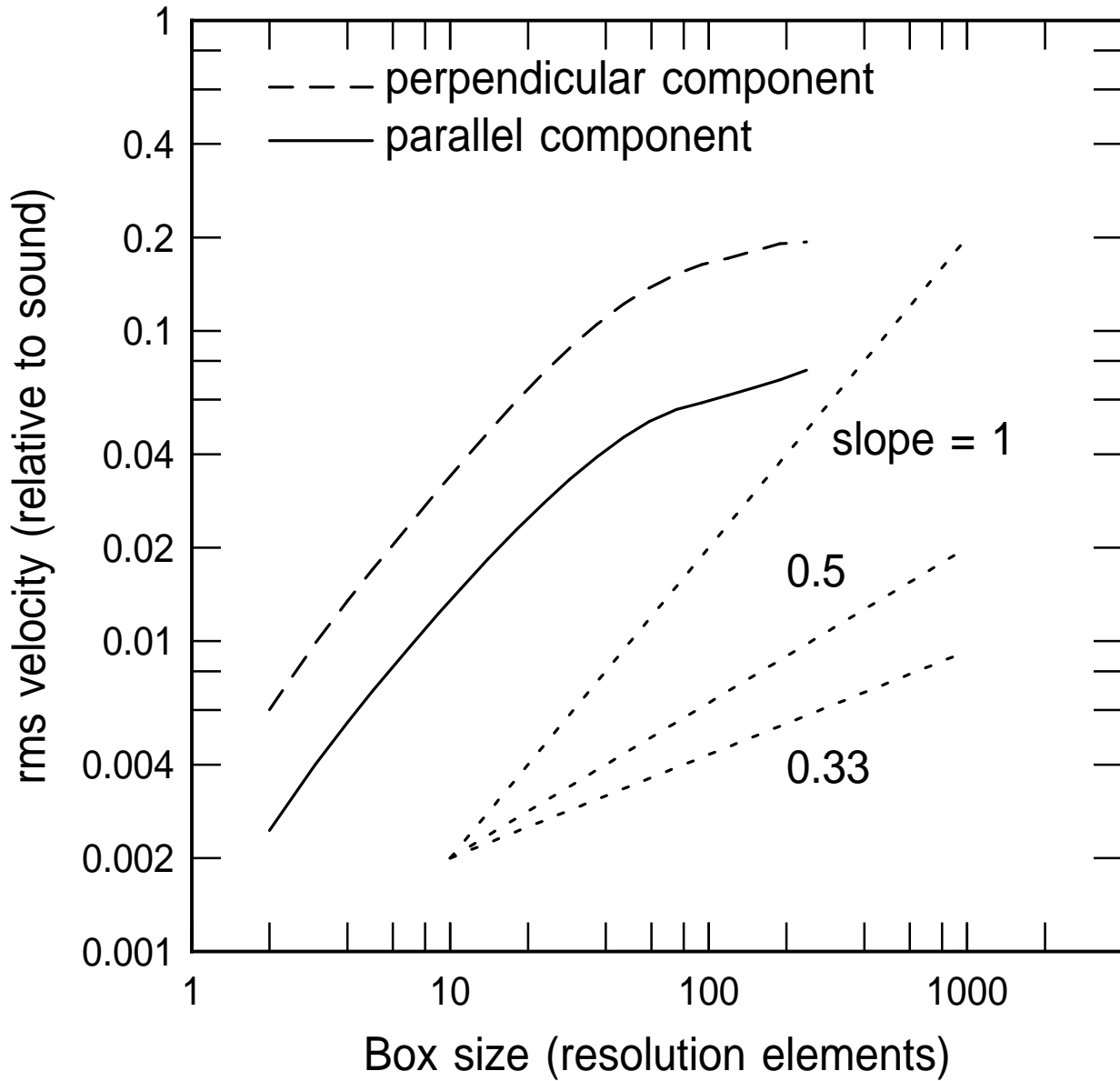


Fig. 8.— The rms velocity in boxes of various sizes is shown versus the box size for the simulation in figure 5. This diagram indicates that the motions in the simulation are correlated with a velocity-size relation given by a power law with power $\sim 1/3$ for scales larger than ~ 30 cells, and with steeper power, ~ 1 on smaller scales. The grid boundaries are on much larger scales, 640 and 800, so edge effects are not important here.

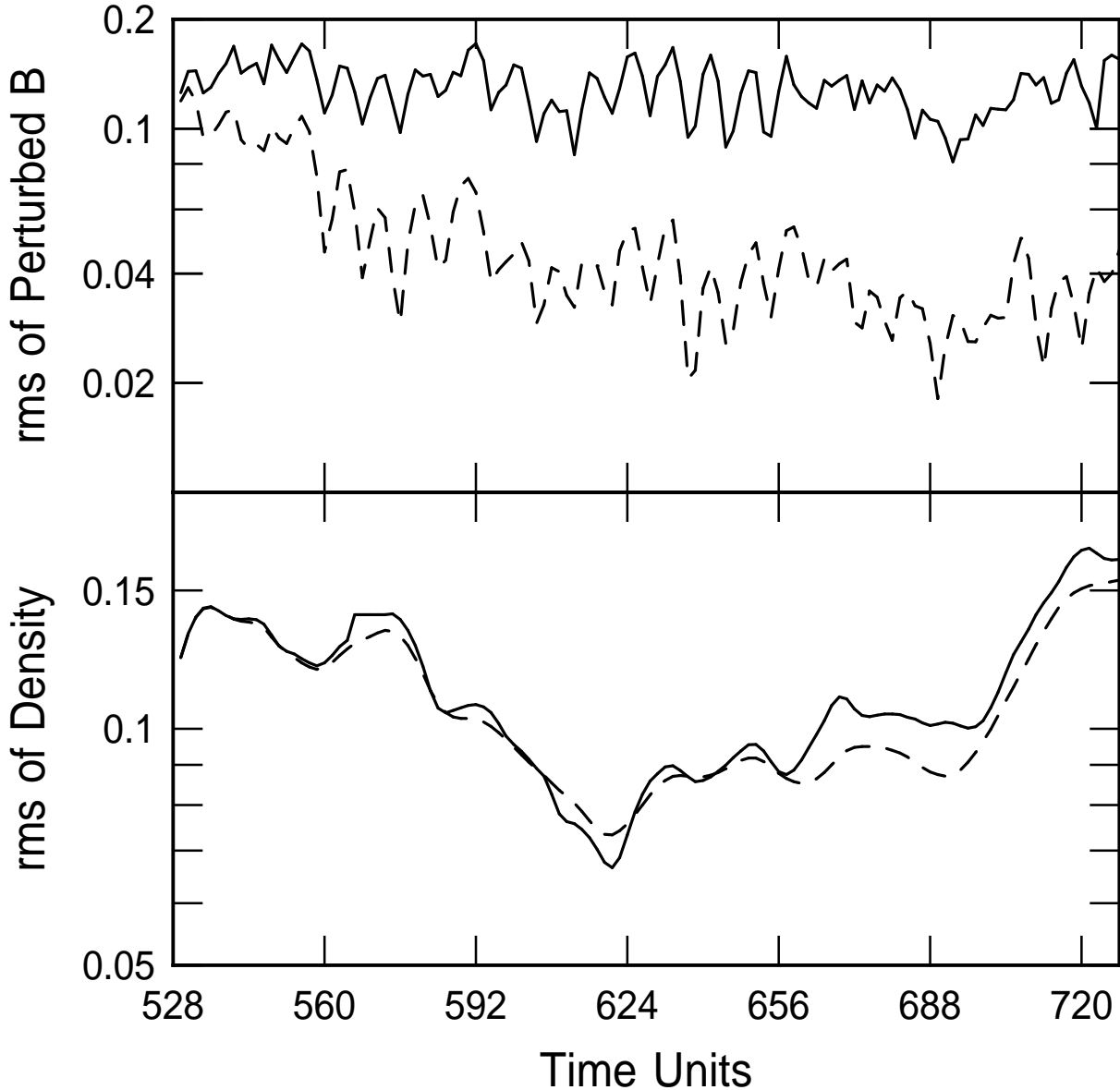


Fig. 9.— The rms deviations around the mean, measured perpendicular to the initial magnetic field, for density at the bottom of the figure and perpendicular component of the field strength at the top, for two runs with different magnetic diffusion rates. The dashed line has more magnetic diffusion by a factor of 10 than the solid line. Enhanced magnetic diffusion decreases the strength of the magnetic waves inside the cloud without affecting the density structure.

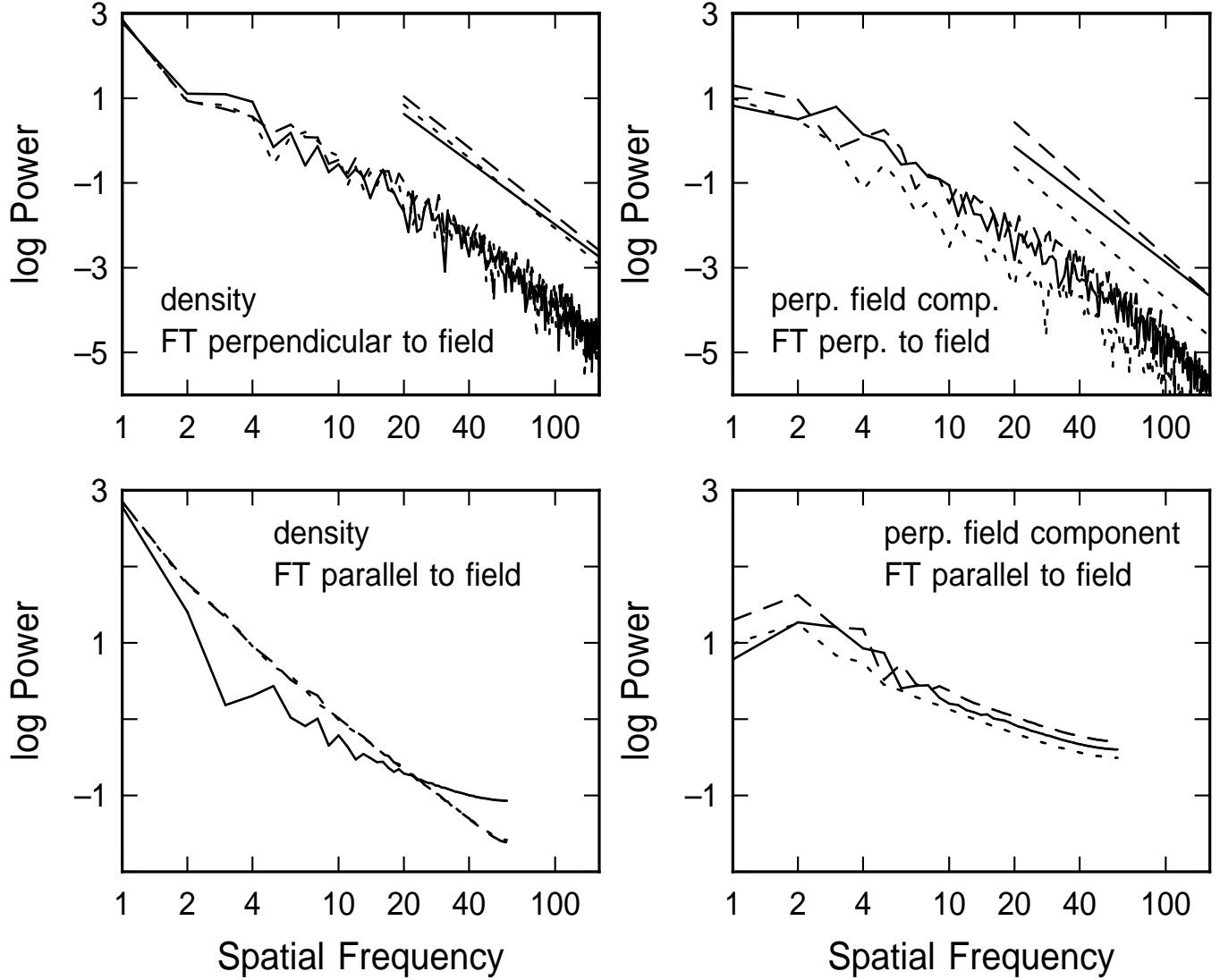


Fig. 10.— The power spectra of density on the left and perpendicular component of the magnetic field strength on the right, measured in directions parallel and perpendicular to the initial field in the bottom and top. The three line types correspond to the beginnings and ends of two simulations: The solid curves correspond to times when the two simulations have just completed identical initial cloud formation phases. The dashed curve is at the end of one of the simulations, following a continuation of the same slow magnetic diffusion. The dotted curve is at the end of the other simulation, which had 10 times faster magnetic diffusion during the last part. The straight lines with the same line types show least squares solutions over the indicated ranges of spatial frequency, shifted upwards by a factor of 100 for clarity. Only the wave amplitude measured by the top right diagram shows any significant change with the enhanced diffusion. The density structure is relatively unchanged when the diffusion rate increases.

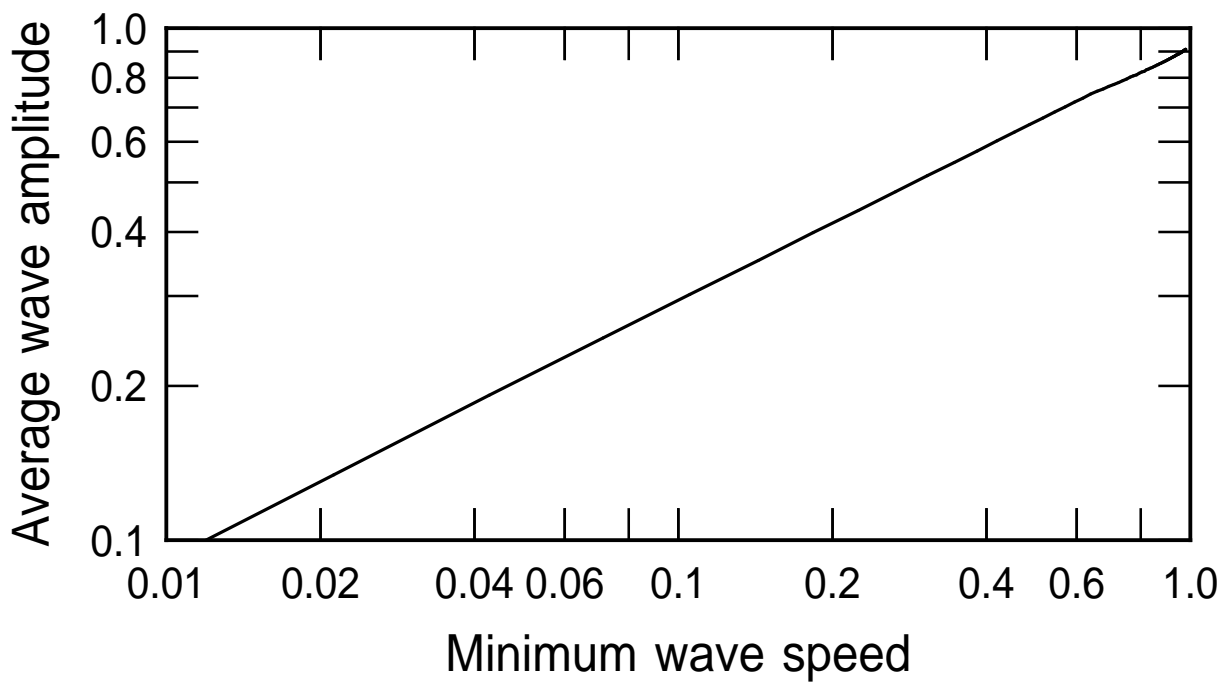


Fig. 11.— The average wave amplitude inside one scale height is shown versus the minimum wave speed at the center of the coordinate system for a WKB solution of a wave propagating into a region with a central depression in the wave speed.

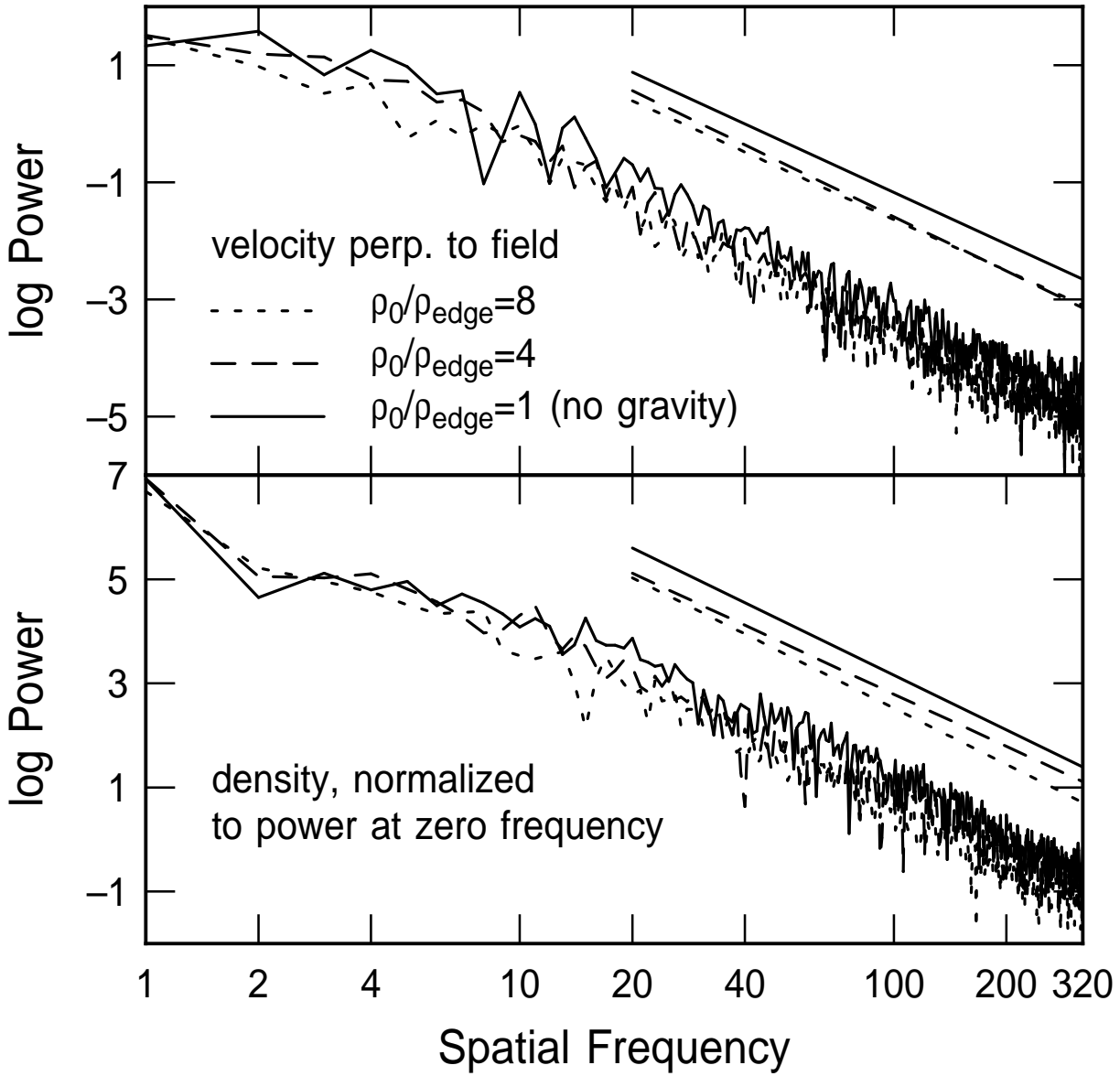


Fig. 12.— Power spectra of density, in the bottom diagram, and perpendicular velocity in the top, measured perpendicular to the field, for three simulations with varying amounts of central density concentration produced by fixed, plane-parallel, gravitational fields. The density power spectrum is normalized to the power at 0 spatial frequency. The solid curve is the same simulation shown in figure 5, with no gravity and an initially uniform density. The dashed curve has an initial equilibrium density enhancement in the center of the grid that is a factor of 4 over the density at the edge, where the waves are generated. The dotted curve has a factor of 8 equilibrium density enhancement. The straight lines are least-squares fits to the power spectra, shifted upwards by factors of 100 for clarity. The simulations with enhanced central densities have weaker waves and smoother density structures than the initially uniform solution, as shown by the smaller power in the dashed and dotted lines compared to the solid lines.